Fabrication and Characterization of Optoelectronics Devices Based on III-V Materials for Infrared Applications by Molecular Beam Epitaxy

Amin Torfi

Submitted in partial fulfillment of the
requirements for the degree of
Doctor of Philosophy
in the Graduate School of Art and sciences

COLUMBIA UNIVERSITY

2012

ABSTRACT

"Fabrication and characterization of optoelectronic devices based on III-V materials for infrared applications by molecular beam epitaxy"

Amin Torfi

Optoelectronic devices based on III-V materials operating in infrared wavelength range have been attracting intensive research effort due to their applications in optical communication, remote sensing, spectroscopy, and environmental monitoring. The novel semiconductor lasers and photodetectors structures and materials investigated in this thesis cover the spectral range from 1.3µm to 12µm. This spectral region includes near-infrared (NIR), mid-infrared (MIR) and long wavelength infrared.

This thesis demonstrated infrared optoelectronic devices, based on III-V compound semiconductors grown by Molecular Beam Epitaxy (MBE,) utilizing various combinations of novel III-V materials, device structures and substrate orientations.

This thesis will be presented in two parts; the first part focuses on two types of photodetectors; type-II InAs/GaSb superlattice IR detector and AlGaAsSb/InGaAsSb mid-infrared heterojunction p-i-n photodetector. The second part of this thesis focuses on the three types of quantum well (QW) lasers; phosphor-free1.3µm InAlGaAs strain-compensated multiple-quantum-well (SCMQW) lasers on InP (100), InGaAsNSb/GaAs quantum wells (QWs) grown on GaAs (411)A substrates and mid-infrared InGaAsSb lasers with digitally grown tensile-strained AlGaAsSb barriers.

Type-II InAs/GaSb superlattice IR detectors with various spectral ranges were grown by MBE. Two superlattice structures with 15 monolayers (ML) of InAs/12ML GaSb and 17ML InAs/7ML GaSb are discussed. Based on X-ray diffraction (XRD) measurements both InAs/GaSb superlattices exhibit excellent material qualities with the full width at half maximum (FWHM) of the 0th-order peak about 20arcsec, which is among the narrowest ever reported. The 50% cutoff wavelengths at 80K of the two photodiodes with 15ML InAs/12ML GaSb and 17ML InAs/7ML GaSb superlattices are measured to be 10.2μm and 6.6μm, respectively.

Mid-infrared heterojunction p-i-n photodetector, AlGaAsSb/InGaAsSb lattice-matched to GaSb grown by solid source molecular beam epitaxy using As and Sb valved crackers greatly facilitated the lattice-matching of the quaternary InGaAsSb absorbing layer to the GaSb substrates, as characterized by X-ray diffraction. The resulting device exhibited low dark current and a breakdown voltage of 32V at room temperature. A record Johnson-noise-limited detectivity of 9.0×10^{10} cm $Hz^{½}$ /W was achieved at 290K. The 50% cutoff wavelength of the device was 2.57 μm. Thus, our result has clearly demonstrated the potential of very high-performance lattice-matched InGaAsSb p–i–n photodetectors for mid-infrared wavelengths.

For phosphor-free1.3 μm InAlGaAs multiple-quantum-well (MQW) lasers, the substrate temperature has been found to be a critical growth parameter for lattice-matched InAl(Ga)As layers in the laser structures. As shown by X-ray diffraction measurements, in the temperature range of 485–520° C, spontaneously ordered superlattices (SLs) with periods around 7–10 nm were formed in the bulk InAl(Ga)As layers. Based on photoluminescence (PL) measurements, a large band gap reduction of 300 meV and a broadened PL peak were observed for the $In_{0.52}Al_{0.48}As$ layers with SL, as compared to those without SL. The undesirable, spontaneously-

ordered SL can be avoided by using MBE growth temperatures higher than 530 °C. This results in a high laser performance. Threshold-current density as low as 690 A/cm² and T_0 as high as 80 K were achieved for InAlGaAs laser bars emitting at 1310 nm.

InGaAsNSb/GaAs QWs on GaAs (411)A exhibited remarkably enhanced photoluminescence efficiency compared with the same structures on conventional GaAs (100) substrates. It was further observed that the optimum growth temperature for (411)A was 30 °C higher than that for (100). To explain this phenomenon, a model based on the self-assembling of local rough surface domains into a unique global smooth surface at the lowest energy state of the system is proposed.

Lastly, the digital-growth approach for tensile-strained AlGaAsSb barriers improved the reliability and controllability of MBE growth for the MQW active region in the mid-infrared InGaAsSb quantum well lasers. The optical and structural qualities of InGaAsSb MQW were improved significantly, as compared to those with random-alloy barriers due to the removal of growth interruption at the barrier/well interfaces in digital growth. As a result, high-performance devices were achieved in the InGaAsSb lasers with digital AlGaAsSb barriers. A low threshold current density of 163 A/cm² at room temperature was achieved for 1000-μm-long lasers emitting at 2.38 μm. An external differential quantum efficiency as high as 61% was achieved for the 880-μm-long lasers, the highest ever reported for any lasers in this wavelength range.

Table of Contents

Acknowledgments

I would first like to thank my advisor Professor Wen I Wang, who introduced me to the field of semiconductor physics and devices. This thesis would not be completed without his continues support and guidance. All the skills and knowledge I have gained throughout the entire research are the result of his encouragement, inspiration and support; I owe him a deep sense of gratitude.

I also would like to thank my colleagues whom I worked with in this group including: Dr. Weiping Li, Dr. Hui Shao, Dr. Grayson Chen, Cheng-Yun Chou, and Dr. Fernando Guarin and Dr. Chengwen Pei (both at IBM Microelectronics Lab and alumni of this group who visited this group often as collaborators). I am thankful for all of their collaborations, assistance and helpful discussions.

Finally, I would like to thank all my family members for their love and supports.

Chapter 1

Introduction

1.1 Historical Background

Semiconductor lasers have assumed an important technological role since their invention in the early sixties.[1−4] The main factors driving the surge in the role played by semiconductor lasers are: the invention of semiconductor injection lasers; the achievement of semiconductor double-heterostructure (DHS) laser; the achievement of semiconductor quantum-well (QW) lasers and the extensive development of strained quantum-well (QW) lasers.

Prior to 1962, the important theoretical concepts such as "Light Amplification by Stimulated Emission of Radiation",[5] "Quasi-Fermi Levels",[6] "Population Inversion",[6] and "Resonant Cavity"[7] in semiconductor lasers were developed. The semiconductor optoelectronics started its rapid growth when in the late 1962, the research group from IBM, General Electronics and MIT Lincoln Laboratory in U.S. independently reported the invention of homojunction semiconductor injection lasers.[8−11] The semiconductor laser based on GaAs and GaAsP p-n homojunctions showed extremely high threshold current density (in order of tens of kA/cm^2) and low working temperature (77K). The p-n junctions in the first semiconductor lasers were fabricated by diffusion.

Improving the performances of semiconductor laser by employing semiconductor double-heterostructure (DHS) [12,13] has driven tremendous advancements in this area. Kroemer and Alferov independently proposed to improve the performances of semiconductor laser by employing semiconductor double-heterostructure (DHS) immediately after the achievement of semiconductor homojunction lasers. Compared to p-n homojunction lasers, semiconductor hetrojunctions provided three very important properties for semiconductor lasers: 1) super

injection of carries, 2) improved current confinement and 3) stronger optical confinement in active region.

Low threshold (in the order of 1 kA/cm^2) and room-temperature (RT) continuous-wave (CW) semiconductor lasers were achieved during 1969-1970 by using almost lattice-matched AlGaAs/GaAs/AlGaAs heterostructures.[14] Achievement of CW RT lasing stimulated the explosion of interest in physics and technology of semiconductor heterostructures. At this era, semiconductor heterostructures were fabricated by liquid phase epitaxy (LPE) and were limited to latticed-matched AlGaAs/GaAs system.

The revolutionary technique using Molecular beam epitaxy (MBE)[15,16] and metal organic chemical vapor deposition (MOCVD)[17] in 1970s, broke new ground in the growth of ultrathin semiconductor layers, on the order of ten atomic layers, and have laid the foundation for the development of the quantum well (QW)[18–22] laser. The reduction of the confinement factor for electron-hole pairs to a tiny volume in QW improved the laser performance and reduced threshold current density to as low as 500 A/cm².[23]

Strained quantum-well lasers were proposed by Adams, Yablonovitch and Kane in 1986.[24,25] In their predictions, the strain modification in semiconductor QW should have significant benefits for lasing performances, including reduced threshold current density, enhanced dynamic response and high-speed performance. In the following years, intensive effort has been made to explore the high performances brought by strained QW structure in different material systems including InGaAs/GaAs, InGaAs/InP by using various epitaxial methods.[26–28] In 1990s, the interest in strained QW lasers became even more intensive and a number of

material systems were investigated to cover wavelength range from ultra-violet (UV) to mid-infrared (MIR) wavelength range.[27−31]

Furthermore, there has been an increasing interest in infrared (IR) detectors fabricated from semiconductor quantum wells (QWs) and superlatices. This is because modern crystal growth techniques, such as molecular beam epitaxy (MBE) and metal organic chemical vapor deposition (MOCVD) have made it possible to grow semiconductor thin films with precise control of composition, doping and thickness.[32−34]

The development of strained layer superlattices has largely been motivated by the promise of overcoming fundamental and practical limitations of conventional infrared (IR) detectors such as those based on HgCdTe or extrinsic Si. A mature superlattice technology has eased the detector cooling requirements, provided higher performance at a fixed operating temperature, and demonstrated both uniformity and producability superior to that of intrinsic detectors.[33,34]

Semiconductor lasers are attractive for research because they are technologically important and vital applications drive the need for better and newer lasers, which generate more applications, which in turn support the development of even better and more versatile lasers. This is especially true of quantum well lasers. In spite of being a well established commercial device already used in many applications, high-performance strained QW lasers will still be the subject of intense research and development, perhaps for years to come.

1.2 General Motivation

Light sources emitting at infrared (IR) wavelengths are of a growing interest due to their potential applications in telecommunications, molecular spectroscopy and airborne countermeasures. These applications require mid-IR laser sources with rather demanding attributes, such as wide tunability, narrow linewidth, portability, room-temperature operation and high output power.

Many biological molecules and chemical gases have distinctive absorption lines associated with the transitions between different energy levels of the molecules. Most of these absorption lines located in the infrared spectral range between 2 to 5μm. Therefore the mid-infrared is preferred for spectroscopic detection because it contains the most important fundamental absorption band of the atmospheric trace gases, such as NO, CF_4, NH_3, and most hydrocarbons. Fig-1.1 shows the absorption intensity of several major gas molecules extracted from the HITRAN database.[35]

Other applications require very high output power. Typical examples are laser radar systems, remote sensing and airborne countermeasures. These systems could take advantage of the atmospheric windows at 3-5 μm and 8-12 μm and require mid-IR sources with very high output power, but still require portability and room temperature operation. High beam quality, compact size and robustness are also desirable traits.

Optoelectronics operating in IR wavelengths continue to attract considerable interest as a viable means for alleviating many of the limitations of purely electronic devices. Given the development of MBE and characterization of material quality, as well as determination of band offsets and surface reactivity, the two main thrusts of this thesis research were to improve the

material quality of martial grown by MBE and to expand the arena of III-V based devices to include new devices that take advantage of the unique properties of the materials belonging to this martial group.

For material growth in this thesis, we utilized MBE because the slow growth rate of 0.1-2.0 μm/hr permits very precise control of layer thickness in the sub-micron range. Additionally, the reduced growth temperature, e.g. 500-600°C for GaAs, is low enough not to disturb abrupt compositional or doping profiles because of negligible bulk diffusion and a specific non-equilibrium growth mechanism is responsible for progressive smoothing of the surface for most substrate orientations.

1.3 Organization of Thesis

This thesis is further organized as follows: Chapter 2 describes type-II InAs/GaSb superlattice IR detector with various spectral ranges grown by MBE is discussed. Two superlattice structures with 15 monolayers (ML) InAs/12ML GaSb and 17ML InAs/7ML GaSb are demonstrated. The X-ray diffraction (XRD) measurements show that both InAs/GaSb superlattices exhibit excellent material qualities.

Chapter 3 describes the AlGaAsSb/InGaAsSb p-i-n photodetector lattice-matched to GaSb grown by solid source molecular beam epitaxy using As and Sb valved crackers which greatly facilitated the lattice-matching of the quaternary InGaAsSb absorbing layer to the GaSb substrates.

Chapter 4 describes the 1.3 μm InAlGaAs strain-compensated multiple-quantum-well lasers (SCMQW) without any phosphor-containing layers in the epitaxial structure, which have been grown by molecular-beam epitaxy (MBE). The chapter demonstrates how the substrate temperature was found to be a critical growth parameter for lattice-matched InAl(Ga)As layers in the laser structures which resulted.

In Chapter 5 the InGaAsNSb/GaAs QWs grown on GaAs (411)A substrates by MBE is discussed. This chapter provides the analysis for InGaAsNSb/GaAs QWs on GaAs (411)A which exhibited remarkably enhanced photoluminescence efficiency compared with the same structures on conventional GaAs (100) substrates.

Chapter 6 describes the InGaAsSb lasers emitting in the mid-infrared (MIR) with strain-compensated multiple-quantum-well (SCMQW) active region have been grown by MBE. This

chapter demonstrates how digitally grown tensile-strained AlGaAsSb was employed as barriers to increase the valence-band offset for hole confinement.

Chapter 7 summarizes key takeaways and concludes the work in this thesis.

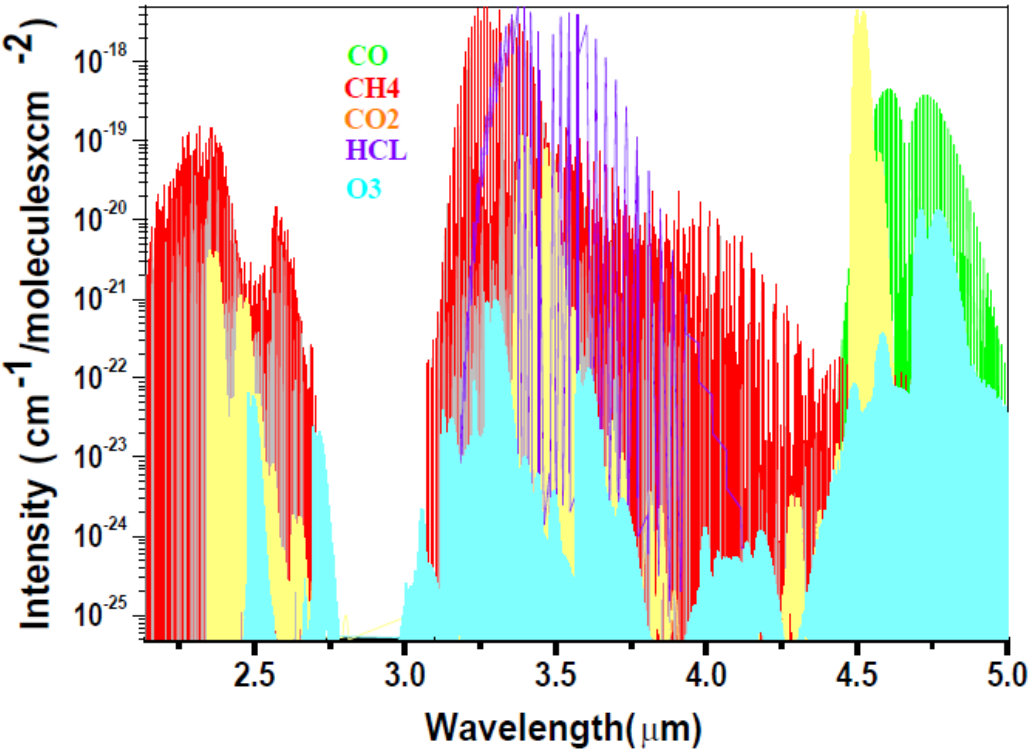

Fig. 1.1 Absorption intensity of several major gas molecules extracted from the H ITRAN database.

References

1. Hall, R. N., Fenner, G. E., Kingsley, J. D., Soltsy, T. J., ans Carlson, R. O. (1962). Phys. Rev. Lett., 9, 366.
2. Holonyak, N. Jr. and Bevacqua, S. F. (1962). Appl. Phys. Lett., 1, 82.
3. Nathan, M. I., Dumke, W. P., Burns, G., Dill, F. H. Jr., and Lasher, G. (1962) Appl. Phys. Lett., 1, 62.
4. Quist, T. M., Rediker, R. II., Keyes, R. J., Krag, W. E., Lax, B., McWhorter, A. L., and Zeigler, H. J., (1962). Appl. Phys. Lett., 1, 91.
5. J. von Neumann "Notes on photo-disequilibrium-amplification scheme" an unpublished manuscript written before Sep. 16, 1953. Recollected in IEEE, J. Quantum electron. 23, 659, (1987).
6. M.G.A. Bernard and G. Durafourg, Phys. Stat. Sol., 1, 699, (1961).
7. N.G. Basov, O.N. Krokhim, and Yu. M. Popv, Sov. Phys. JEPT, 13, 1320, (1961).
8. R.N. Hall, G. E. Fenner, J.D. Kinsley,T. J. Soltys, and R.O. Carlson , Phys. Rev. Lett., 9, 336, (1962).
9. M.I. Nathan, W.P. Dumke, G. Burns, F.H. Dill, Jr., and G. Lasher, Appl. Phys. Lett., 1, 62, (1962).
10. N.Holonyak, Jr. and S.F. Bevacua, Appl. Phys. Lett., 1, 82, (1962).
11. T.M. Quist, R.H. Rediker, R.J. Keyes, W. E. Krag, B. Lax, A.L. McWhorter, and H.J. Zeiger, Appl. Phys. Lett., 1, 91, (1962).
12. H. Kroemer, Proc. IEEE 51, 1782, (1963).
13. Zh. I. Alferov, V. M. Andreev, E.L. Portoni, and M. K. Trukan, Sov. Phys. Semicond.3, 1107, (1970).
14. I. Hayashi, M.B. Panish, P.W. Foy, S. Sumski, Appl. Phys. Lett., 17, 109, (1970).
15. A. Y. Cho, J. Vac. Sci., 8, S31, (1971).

16. A. Y. Cho, R. W. Dixon, H. C. Casey, Jr., and R. L. Hartman, Appl. Phys. Lett., 28, 501(1976).

17. R. D. Dupuis, and P. D. Dapkus, Appl. Phys. Lett., 31, 466(1977).

18. J. P. Van Der Ziel, R. Dingle, R. C. Miller, W. Wiegmann, and W. A. Nordland, Jr., Appl. Phys. Lett., 26, 463(1975).

19. R. D. Dupuis, and P. D. Dapkus, N. Holonyak, Jr., E. A. Rezek, and R. Chin, Appl. Phys. Lett., 32, 295, (1978).

20. R. D. Dupuis, and P. D. Dapkus, N. Holonyak, Jr., and R. M. Kolbas, Appl. Phys. Lett., 35, 221, (1979).

21. W. T. Tsang, Appl. Phys. Lett., 39, 134, (1981).

22. I. Suemune, L. A. Coldren, M. Yamanishi, and Y. Kan, Appl. Phys. Lett., 53, 1378, (1988).

23. A.R. Adams, Electron. Lett., 22, 249, (1986)

24. E. Yablonovitch, and E. O. Kane, J. Lightwave Technol., 4, 504, (1986).

25. I. Sumune, L. A. Coldren, M. Yamanishi, and Y. Kan, Appli. Phys. Lett., 53, 1387, (1988).

26. K. Y. Lau, S. Xin, W. I. Wang, N. Bar-Chaim, and M. Mittelstein, Appl. Phys. Lett., 55, 1173, (1989).

27. A, Chiti, and E. P. O'Reilly, and A. R. Adams, Electron. Lett., 25, 821, (1989).

28. H.K. Choi and S. J. Eglash, Appl. Phys. Lett., 61, 1154, (1992).

29. C.E. Zah, R. Bhat, B.N. Pathak, F. Favier, W. Lin, M.C. Wang, N.C. Andreadakis, D.M. Hwang, M.A. Koza, T.P. Lee, Z. Wang, D. Darby, D. Flanders, and J.J. Hsieh, IEEE J. Quantum Electron. 30, 511, (1994).

30. S. Nakamura, M. Senoh, S. Nagahama, N, Iwasa, T. Yamada, T. Matsuhita, and H. Kiyoku, and Y. sugimoto, Jpn. J. Appl. Phys. Part II, 35, L74, (1996).

31. M. Knodow, K. Uomi, K. Hosomi, and T. Mozume , Jpn. J. Appl. Phys. 33, L1056 (1994).

32. J. L. Johnson, L. A. Samoska, A. C. Gossard, J. L. Merz, M. D. Jack, G. R. Chapman, B. A. Baumgratz, K. Kosai, and S. M. Johnson, Appl. Phys. Lett., 80, 1116, (1996).

33. H. Mohseni, A. Tahraoui., J. Wojkowski, M. razeghi, G. J. Brown, and W. C. Mitchel, Y. S. Park, Appl. Phys. Lett., 77, 1572, (2000).

34. F. Fuchs, U. Weimer, W. Pletschen, J. Schmitz, E. Ashswede, M. Walther, J. Wagner, and P. Koidl, Appl. Phys. Lett., 82, 4411, (2003).

35. L. S. Rothman et al., J. Quant. Spectrosc. Radiant. Transfer., 96, 139, (2005)

Chapter 2

Type-II InAs/GaSb superlattices grown by molecular beam epitaxy for infrared detector applications

2.1 Introduction

The type-II superlattice has recently been improved substantially and proven itself to be a practical alternative to the state-of-the-art mercury cadmium telluride, HgCdTe (MCT) technology. Type-II superlattice has demonstrated its flexibility in controlling the electronic band structure in addition to creating sophisticated heterostructure designs, which made achieving performance levels comparable to that of HgCdTe (MCT) possible.[1, 2] Furthermore, significantly improved material quality has allowed for the achievement of high quantum efficiency. [3, 4] Type-II InAs/GaSb SLs were first proposed by Esaki et al. in the 1970s [5] and in late 1980s [6] Smith and Mailhiot further applied these type of SLs for broader infrared detection applications. It is important to note that such superlattices were not improved to the level necessary for practical IR detector applications until the growth of high-quality materials became practical in recent years by advanced MBE technologies.[7-10] Compared with HgCdTe (MCT) used in the traditional detector, this InAs/GaSb type-II superlattice (SL) has several important advantages which include larger effective masses of electrons and holes, significantly suppressing tunneling leakage currents and Auger recombination, [11,12] and excellent SL bandgap uniformity over a relatively larger wafer area. [13] Moreover, the effective energy bandgap is tunable by controlling the thickness of InAs and GaSb layers over the mid to long infrared spectral wavelength range (3μm-30μm). Recently, intensive studies have focused on the performance of photodetectors and the development of multi-spectral focal plane arrays (FPAs) for infrared imaging.[14] High performance FPAs have been reported for the wavelengths ranging from the mid-infrared (MWIR) to the long wavelength infrared regime[15] and MWIR/MWIR dual spectral FPAs.[16-18] With spectral tunability and the recently reported considerable progress, the type-II InAs/GaSb

superlattice has become comparable to the HgCdTe (MCT) material for the third-generation multi-spectral infrared detecting systems. [19]

For type-II InAs/GaSb superlattice detectors, Wei *et al.* reported that the 17 ML InAs/7ML GaSb superlattices photodetectors had a 50% cutoff wavelength of 18.8 μm[20]. In this paper, we have conducted further research extensively and report the more accurate results on type-II InAs/GaSb superlattice IR detectors with high detectivities at various spectral ranges. Two type-II superlattice structures with 15 monolayer (ML) InAs/12ML GaSb and 17ML InAs/7ML GaSb were grown on GaSb (100) substrates by solid-source molecular beam epitaxy (MBE).

2.2 Experiments

All the type-II superlattice samples were grown in a Varian Gen-II solid-source MBE system equipped with As and Sb crackers. The growth temperature was kept at 395˚C. The III/V ratios and shutter sequences have been optimized in order to achieve a good material quality and a smooth surface morphology. During the crystal growth of the superlattice, we observed that saturating the growing surface with Sb flux, thus creating the InSb-like InAs/GaSb heterointerface, was critical for achieving high quality materials with superior detector performance. [21] The superlattice photodiode structure contains a 1000 nm GaSb buffer layer, a contact layer doped with Be ($p\sim2\times10^{18}$ cm^{-3}), and a 100-period undoped InAs/GaSb superlattice layer. The 100-period undoped superlattice was grown on top of the buffer layer and acted as the intrinsic layer in the p-i-n structure, and finally, a 50-period Te doped ($n\sim1\times10^{18}$ $cm^{-}3$) superlattice was grown and capped with a 250Å InAs:Te ($n\sim4\times10^{18}$ cm^{-3}) layer for the top contact.

Photodetectors were fabricated based on the p-i-n superlattice structure described above using wet chemical etching and a standard photolithographic process. The device mesa was defined by etching down to the GaSb buffer layer using a tartaric/phosphoric acid based solution. Au/Ti layers were evaporated on top of the mesas and on the buffer layer and a liftoff process was employed to form the ohmic contacts. The mesa has a rectangular shape (350μm×270μm) with a window (220μm×270μm) on top of it. No passivation or antireflection dielectric coating was applied to the p-i-n detectors.

Low temperature current-voltage (I-V) characteristics were measured using a HP4145B semiconductor parameter analyzer and a MMR cryogenic system. Absolute spectral responsivity measurements were performed using a Bomem DA8 Fourier Transform Infrared spectrometer

(FTIR) with a KBr beam splitter, a blackbody source maintained at 1000K, and an Ithaco1211 current preamplifier. The measured spectra were background corrected for the optical characteristics of the spectrometer with a reference spectrum.

2.3 Results and Discussions

Two photodiodes structures with 17ML InAs/7ML GaSb and 15 ML InAs/12ML GaSb superlattices were grown by MBE on GaSb (100) substrates. Similar period thicknesses for two superlattices were selected in order to have similar device processing procedures. The structural characteristics of the superlattices were evaluated using a five-crystal high resolution X-ray diffractometer. Fig. 2.1 (a) and (b) show the typical diffraction patterns of the as-grown samples with 17ML InAs/7ML GaSb and 15 ML InAs/12ML GaSb superlattices in the vicinity of the GaSb (400) reflections, respectively. The SLs had a single period thickness of 72Å and 80Å as determined from the average spacing of the satellite peaks in Fig. 2.1 (a) and (b). The lattice mismatches to the substrate of both superlattices were kept in the range of 5×10^{-5}. The diffraction patterns revealed intense and well-resolved satellite peaks demonstrating excellent structural quality. The full-width at half-maximum (FWHM) of the zeroth-order superlattice peak for structures was measured to be 20arcsec and 22arcsec for samples with 17ML InAs/7ML GaSb and 15ML InAs/12ML GaSb superlattices, respectively, which are among the best results reported for this SL material system.

Fig. 2.2 shows the spectral photoresponse curve of the two superlattice photodiodes. The measurements were performed at 80K under zero bias voltage with the photodiodes illuminated from the front side at normal incidence. As shown in the figure, the photodiode with 17ML InAs/7ML GaSb superlattice has spectral response well extended into the 8-12μm atmosphere transparent window. The 50% cutoff wavelength of this photodiode was at 10.2μm. The photodiode with 15ML InAs/12ML GaSb superlattice exhibits most of its spectral response in the mid-infrared range. The 50% cutoff wavelength of this device was at 6.6 μm. The 15ML InAs/12ML GaSb superlattice showed shorter cutoff wavelength because the thinner InAs layer

provided larger quantum confinement energy for electrons. On the other hand, the thickness of GaSb layer influenced the width of the conduction band, and played an opposite role to that of InAs layer in affecting the superlattice band gap.[22] At 80K, a responsivity of 1.8A/W was achieved at the wavelength of 9.0 μm for the photodiode with 17ML InAs/7ML GaSb superlattice, which represented an external quantum efficiency of 25%. For the photodiode with shorter cutoff wavelength, the responsivity at 6.0 μm was measured to be 1.3A/W, corresponding to an external quantum efficiency of 27%.

Fig. 2.3 shows the I-V characteristics of the photodiodes at 80K under dark condition. As illustrated in the figure, the photodiodes with 15ML InAs/12ML GaSb superlattice showed a lower dark current under reversed bias voltages, resulting from the larger band gap of this superlattice. At a reversed bias voltage of 0.20V, the dark current density of the photodiode with 15ML InAs/12ML GaSb superlattice was 4.6 mA/cm^2, which was more than two orders of magnitude lower than that of the 17ML InAs/7ML GaSb photodiode being around 1.0A/cm^2.

The Johnson-noise-limited detectivity (D^*) for the type-II InAs/GaSb superlattice photodiodes at a specific temperature can be evaluated, given the zero bias resistance R_0A and spectral photoresponsivity $R(\lambda)$. [23]

$$D^*(\lambda) = R(\lambda)\sqrt{\frac{R_0 A}{4kT}} \qquad (1)$$

Where k is the Boltzmann constant and T is the operation temperature in degrees of Kelvin. The zero-bias resistance area product (R_0A) can be obtained from the slope of the I-V characteristic near zero bias. Making use of the zero-bias photoresponsivity $R(\lambda)$ and the R_0A for the two photodiodes at 80K, the Johnson-noise-limited detectivities of the two photodetectors

are plotted in Fig. 2.4. The 6 μm detectivity (D^*) of 1.2×10^{11}cmHz$^{1/2}$/W was achieved at 80K for the photodiode with 15ML InAs/12ML GaSb superlattice. This detectivity was on the same order of magnitude as the background limited performance (BLIP) of ideal photovoltaic detector at this wavelength, which is 3×10^{11}cmHz$^{1/2}$/W. For the photodiode with 17ML InAs/7ML GaSb superlattice, the Johnson-noise-limited detectivity of 2.2×10^{10}cmHz$^{1/2}$/W was achieved at 9 μm and 80K.

The operation of the photodiode with 15ML InAs/12ML GaSb superlattice was further evaluated at near room temperatures. Fig. 2.5 (a.) illustrates R_0A plotted against 1000/T for the device. As shown in the figure, the activation energy of about 110meV can be extracted from the slope of the curve at temperature near 240K. It is about 30% smaller than the superlattice bandgap, which is about 150 meV measured around this temperature. This implies that near this temperature, the dark current was mainly dominated by the carrier diffusion mechanism. [24] Carrier generation-recombination (G-R) mechanism also contributed to the dark current of this photodiode. The R_0A was about 4.8Ωcm^2 at 210K. Therefore the resulting 6.0 μm Johnson-noise-limited detectivity at this temperature was 1.2×10^8cmHz$^{1/2}$/W. Fig. 2.5(b) illustrates the Johnson-noise-limited detectivity of the photodiodes as a function of temperature at a wavelength of 6.0 μm.

Fig. 2.6 depicts the spectral responsivity at 6.0 μm and 50% cutoff wavelength of the superlattice photodiode with 15ML InAs/12ML GaSb superlattice, both as functions of temperature from 80K to 280K. As the temperature was decreased, a blue shift of the 50% cutoff wavelength was observed, which corresponded to the reduction of the energy gap of the superlattice. The responsivity at 6.0 μm decreased exponentially as the reciprocal temperature was decreased above 160K, and the curve can be fitted linearly. The activation energy can be

extracted from the slope of the line. [25] The resulting activation energy was 126 meV, close to the measured superlattice bandgap and was consistent with the previous activation energy from the Arrhenius plot of R_0A. The spectral response curves for this unoptimized and unpassivated device were measurable at temperatures up to 280K and 50% cutoff wavelengths up to 8.6 μm, making this device very promising for mid and long infrared wavelength range applications.

3.4 Summary and Conclusion

Type-II InAs/GaSb superlattice IR detectors with various spectral ranges were grown by solid-source molecular beam epilaxy (MBE). Two superlattice structures with 15 ML InAs/12ML GaSb and 17ML InAs/7ML GaSb were demonstrated. The X-ray diffraction (XRD) measurements demonstrated that both InAs/GaSb superlattices exhibited excellent material and interface qualities with the FWHM of the 0th-order peak at 20 arcsec for both superlattices. The 50% cutoff wavelengths at 80K of these two structures were measured to be 6.6 μm and 10.2 μm, respectively. A zero bias Johnson-noise-limited D^* of 1.2×10^{11}cmHz$^{1/2}$/W was achieved at 80K and 6 μm for unpassivated photodiodes with 15ML InAs/12ML GaSb superlattice, while a zero bias Johnson-noise-limited D* of 2.2×10^{10}cmHz$^{1/2}$/W was achieved at 80K and 9 μm for unpassivated photodiodes with 17ML InAs/7ML GaSb superlattice. The operation of the photodiode with shorter cutoff wavelength was investigated up to 280K, which is near room temperatures. The 6 μm zero bias Johnson-noise-limited D* of this photodiode was 1.2×10^{8}cmHz$^{1/2}$/W at 210K.

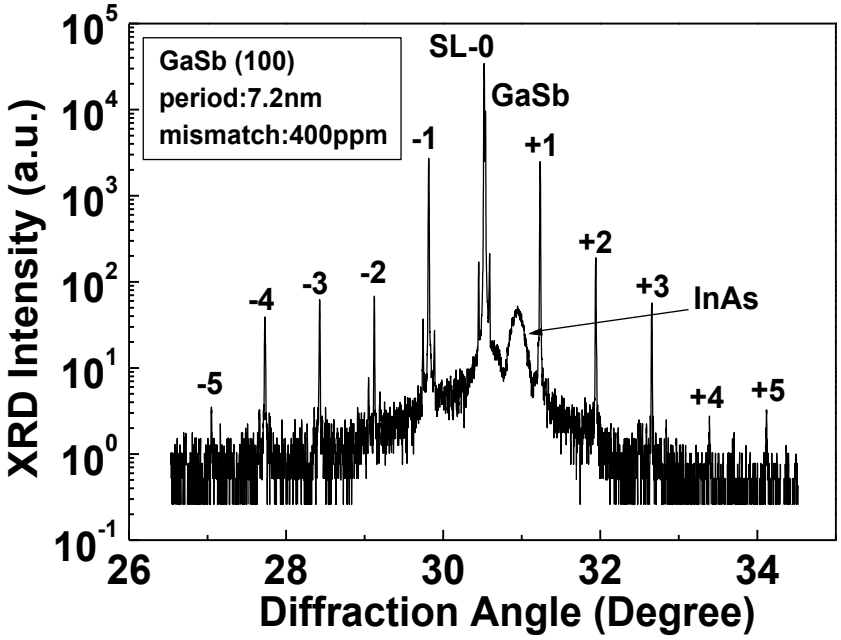

(a)

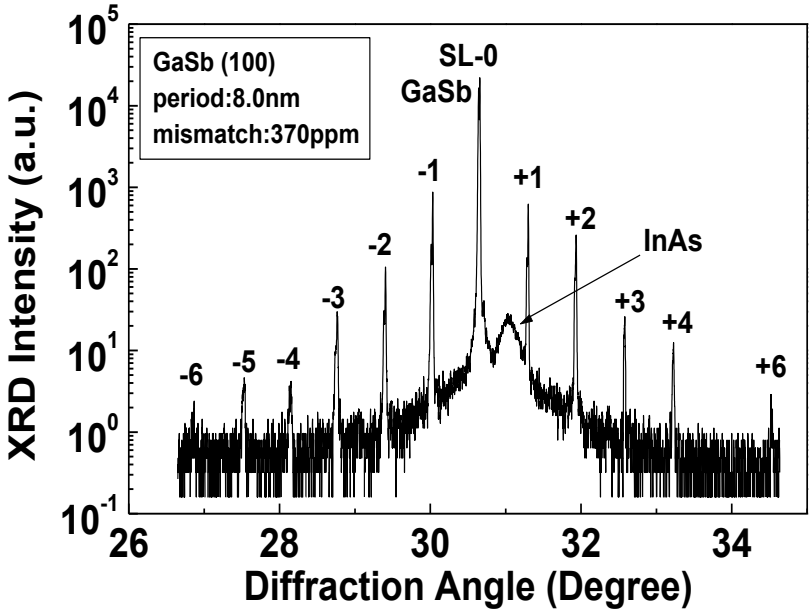

(b)

FIG. 2.1. High-resolution x-ray diffraction patterns of InAs/GaGb superlattice photodetector structures grown on GaSb (100) substrate, (a) 17ML InAs/7ML GaSb superlattice (b) 15ML InAs/12ML GaSb superlattice. FWHMs of the zeroth-order superlattice peak for both structures were around 20 aresec.

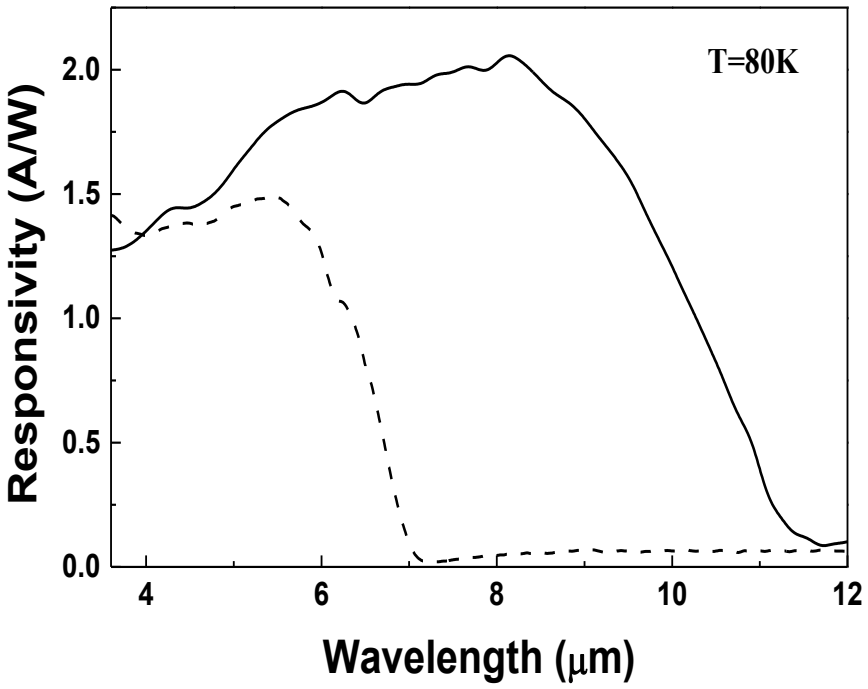

FIG. 2.2. The responsivity spectra of the superlattice photodetectors at 80K under zero bias. The 50% cutoff wavelengths at 80K of the photodiodes with 15ML InAs/12ML GaSb (dash) and 17ML InAs/7ML GaSb (solid) superlattices were measured to be 6.6 μm and 10.2μm, respectively.

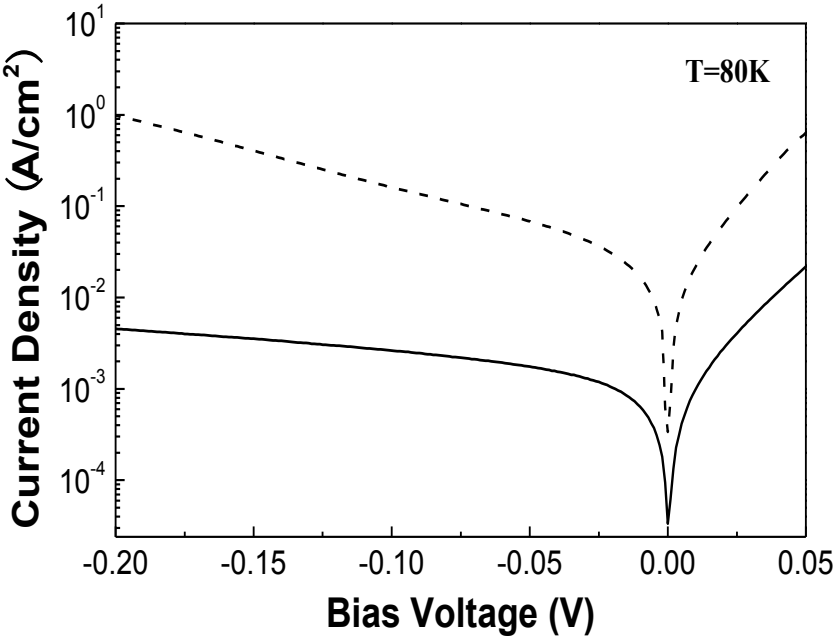

FIG.2.3. Dark current densities at 80K of the unpassivated photodiodes with superlattice structures of 15ML InAs/12ML GaSb (dash) and 17ML InAs/7ML GaSb (solid).

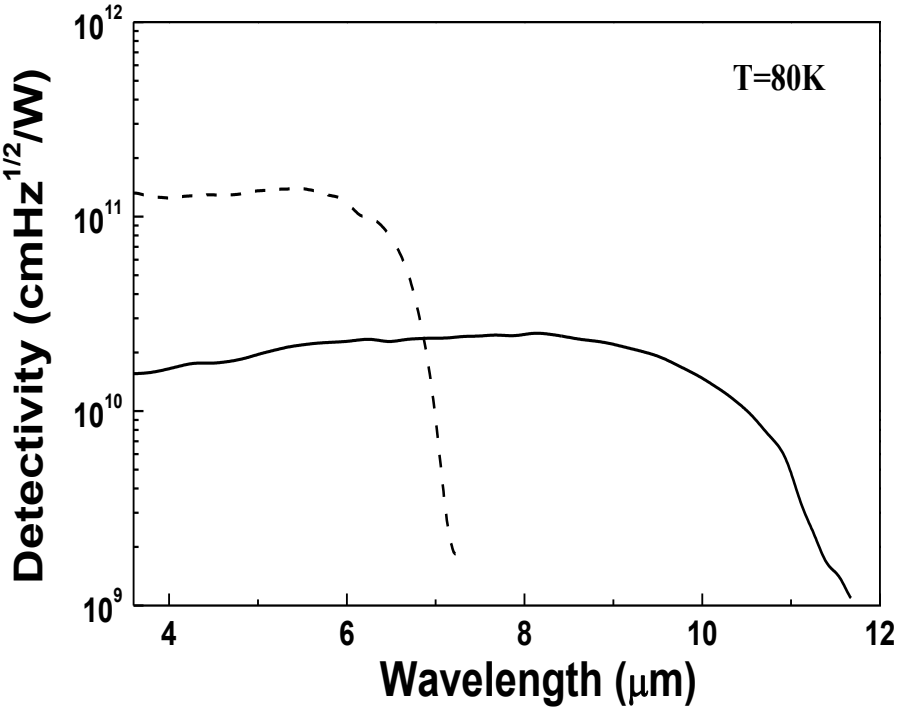

FIG.2.4. Johnson-noise-limited detectivities as a function of wavelength at 80 K and zero bias for the two photodiodes with superlattice structures of 15ML InAs/12ML GaSb (dash) and 17ML InAs/7ML GaSb (solid).

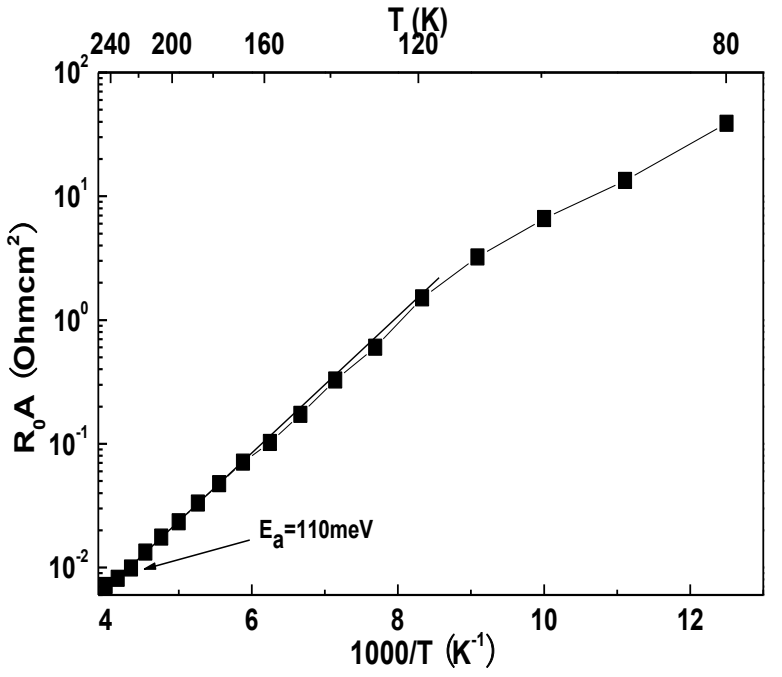

(a)

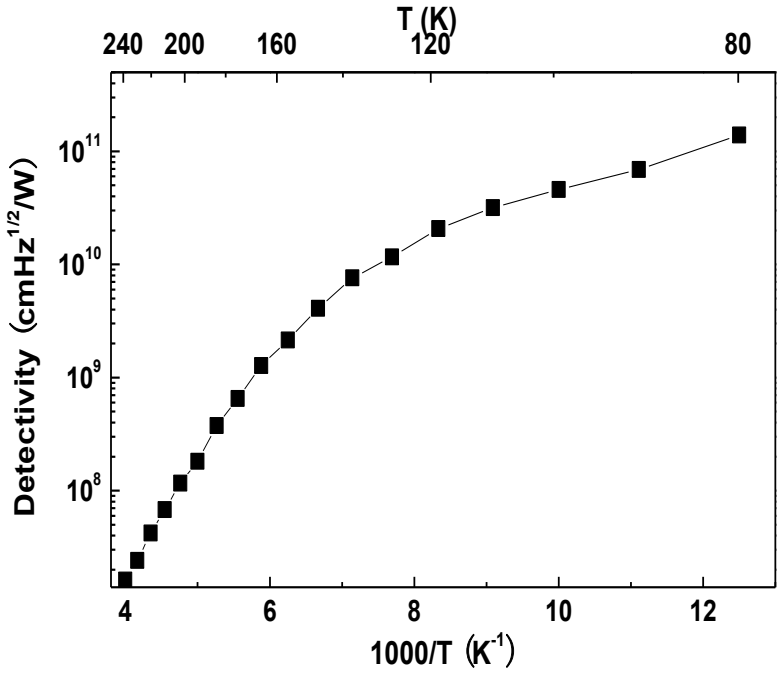

(b)

FIG.2.5. Temperature dependence of the (a) resistance area product (R_0A) and (b) Johnson-noise-limited detectivity (D*) at 6.0 μm for a typical photodiode with 15ML InAs/12ML GaSb superlattice. Activation energy E_a of 110meV was extracted at temperature near 240K.

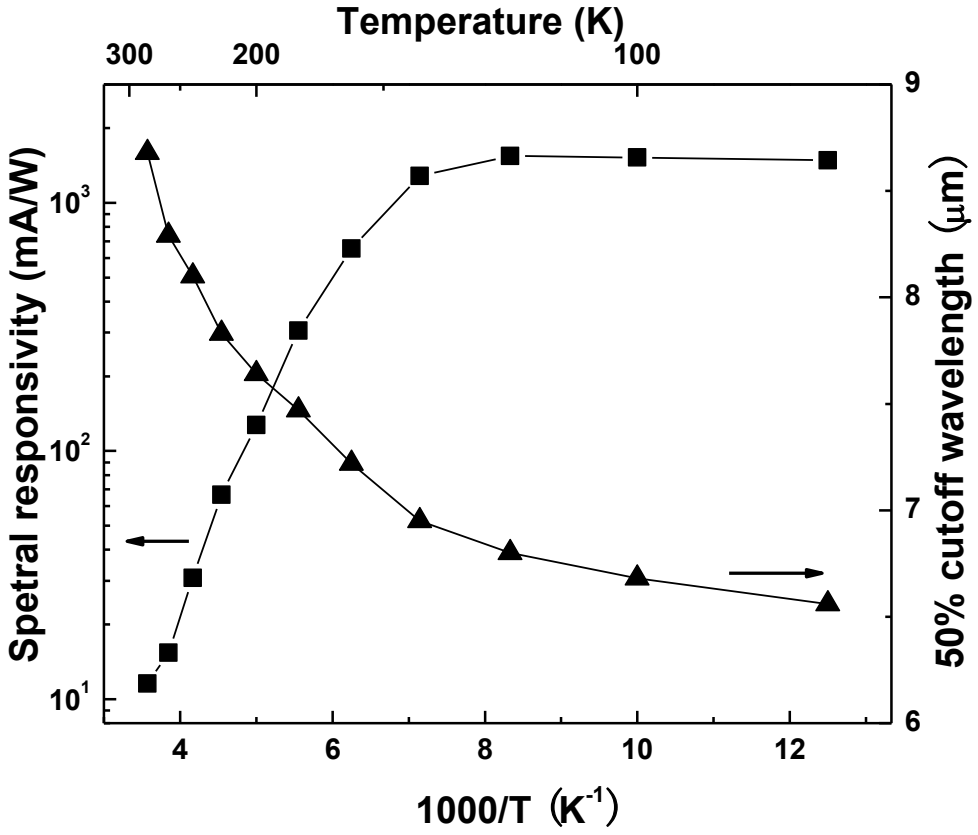

FIG.2.6. Spectral responsivity at 6.0μm and 50% cutoff wavelength as functions of temperature from 280K to 80K for a typical photodiode with 15ML InAs/12ML GaSb superlattice.

References

1. E. H. Eifer, S. I. Maximenko, M. K. Yakes, C. Yi, C. L. Canedy, I. Vurgaftman, E. M. Jackson, J. A. Nolde, C. A. Affouda, M. Gonzalez, J. R. Meyer, K. P. Clark, and P. R. Pinsukanjana, Proceedings of the SPIE, v **7660**, p. 76601Q (2010).

2. N. Gautam, M. Naydenkov, S. Myers, A. V. Barve, E. Plis, T. Rotter,L. R. Dawson, and S. Krishna, Appl. Phys. Lett. **98**(12), 121106 (2011).

3. A. Soibel, D. Z.-Y. Ting, C. J. Hill, M. Lee, J. Nguyen, S. A. Keo, J. M. Mumolo, and S. D. Gunapala, Proceeding of the SPIE, v **7945** (2011).

4. G. J. Sullivan, A. Ikhlassi, J. Bergman, R. E. DeWames, J. R. Waldrop1, C. Grein, M. Flatté, K. Mahalingam, H. Yang, M. Zhong, and M. Weimer, J. Vac. Sci. Technol. B **23**, 1144 (2005)

5. G. A. Sai-Halasz, R. Tsu, and L. Esaki, Appl. Phys. Lett. **30**(12), 651 (1977).

6. D. L. Smith and C. Mailhiot, J. Appl. Phys. **62**, 2545 (1987).

7. H. Mohseni, A. Tahraoui, J. Wojkowski, M. Razeghi, G. J. Brown, W. C. Mitchel, and Y. S. Park, Appl. Phys. Lett. **77**, 1572 (2000).

8. F. Fuchs, U. Weimer, W. Pletschen, J. Schmitz, E. Ahlswede, M. Walther, J. Wagner, and P. Koidl, Appl. Phys. Lett. **82**, 4411 (2003).

9. Y. Wei, J. Bae, A. Gin, A. Hood, M. Razeghi, G. J. Brown, and M. Tidrow, J. Appl. Phys. **94**, 4720 (2003)

10. H. J. Haugan, G .J. Brown, F. Szmulowicz, L. Grazulis, W. C. Mitchel, S. Elhamri, and W. D. Mitchell, J. Cryst. Growth **278,** 198, (2005).

11. E. R. Youngdale, J. R. Meyer, C. A. Hoffman, F. J. Bartoli, C. H. Grein, P. M. Young, H. Ehrenreich, R. H. Miles, and D. H. Chow, Appl. Phys. Lett. **64**, 3160 (1994).

12. C. H. Grein, P. M. Young, M. E. Flatté, and H. Ehrenreich, J. Appl. Phys. **78**, 7143 (1995).

13. H. Mohseni, A. Tahraoui, J. Wojkowski, M. Razeghi, G. J. Brown, W. C. Mitchel, and Y. S. Park, Appl. Phys. Lett, **77**, 1572 (2000).

14. P. Norton, J. Campbell, S. Horn, and D. Reago, Proc. SPIE*,* **4130**, 226 (2000).

15. M. Walther, J. Schmitz, R. Rehm, S. Kopta, F. Fuchs, J. Fleiner, W.Cabanski, and J. Ziegler, J. Cryst. Growth **278**, 156 (2005).

16. S. D. Gunapala, D. Z.Ting, C. J. Hill, J. Nguyen, A. Soibel, S. B. Rafol, S. A. Keo, J. M. Mumolo, M. C. Lee, J. K. Liu, and A. Liao, Proceeding of the 23rd Annual Meeting of the IEEE Photonics Society, p 637-8 (2010)

17. R. Rehm, M. Walther, J. Schmitz, J. Fleiner, J. Ziegler, W. Cabanski, and R. Breiter, Electron. Lett. **42**, 577 (2006).

18. L. Hoglund, A. Soibel, C. J. Hill, D. Z. Ting, A. Khoshakhlagh, A. Liao, S. Keo, M. C. Lee, J. Nguyen, J. M. Mumolo, and S. D. Gunapala, Proc. SPIE Vol. **7780**, 77800D (2010)

19. A. Rogalski, and P. Martyniuk, Infrared Phys. Tech. **48**, 39, (2006).

20. Y. Wei, A. Gin, M. Razeghi, and G. J. Brown, Appl. Phys. Lett. **80**, 3262 (2002).

21. R. H. Miles, J. N. Schulman, D. H. Chow, and T. C. McGill, Semicond. Sci. Technol. **6,** S102, (1993).

22. H. J. Haugan, F. Szmulowicz, G. J. Brown, and K. Mahalingam, Appl. Phys. Lett. **84**, 5410 (2004).

23. J. L. Johnson, L. A. Samoska, A. C. Gossard, J. L. Merz, M. D. Jack, G. R. Chapman, B. A. Baumgratz, K. Kosai, and S. M. Johnson, J. Appl. Phys. **80**, 1116 (1996).

24. G. Marre, B. Vinter and V. Berger, Semicond. Sci. Technol. **18**, 284, (2003).

25. J. B. Rodriguez, P. Christol, F. Chevrier, and A. Joullié, Physica *E* **28**, 128, (2005).

Chapter 3

2.6 μm AlGaAsSb/InGaAsSb photodetectors grown by molecular beam epitaxy

3.1 Introduction

Mid-infrared photodetectors operating in the 2.0–3.0 μm wavelength range have attracted extensive attention in recent years for applications in molecular spectroscopy, blood glucose sensing and laser radar systems. Currently, there are several choices in this wavelength range. HgCdTe and InSb are the most widely used materials for the mid-infrared photon detectors. However, devices based on these materials have intrinsic drawbacks such as inferior material uniformity, low yield and low temperature operation requirement.[1,2] Photodiodes utilizing quantum well structures such as type-II InGaAs/GaAsSb quantum wells have also been reported to operate in this mid-infrared spectral range.[3] Nevertheless, the overall performance of these devices is not yet satisfactory for practical applications at room temperature. InGaAs photodetectors with lattice constant matched to InP are well developed for optical communications in the wavelength range below1.7 μm. Although the cutoff wavelength of this photodetector can be extended up to 2.6 μm by incorporating more In into lattice-matched $In_{0.53}Ga_{0.47}As$,[4] the material quality is considerably degraded due to increased misfit dislocation density introduced by the lattice-mismatch. This consequently leads to larger dark current and higher noise level of the photodetectors.

The quaternary alloy InGaAsSb is a very promising candidate for the development of optoelectronic devices in the near-and mid-infrared wavelength range. Its bandgap wavelength can vary from1.7 up to 4.3 μm with lattice constant matched to GaSb.[5] During the past few years, InGaAsSb photodetectors on GaSb substrate have been reported using different device structures and growth methods.[6−11]Among different growth methods, molecular beam epitaxy(MBE) has several advantages such as lower substrate temperature, non-equilibrium

growth mechanism and precise control of the epilayers and interfaces, making it a preferred choice to achieve high-performance InGaAsSb photodetectors.

In this chapter, AlGaAsSb/InGaAsSb heterojunction photodiodes lattice-matched to GaSb substrate grown by solid source MBE have been demonstrated. The device structure was optimized to achieve high performance at room temperature. The resulting devices exhibited low dark current and a reverse breakdown voltage of 32V at room temperature. The peak external quantum efficiency of the photodiode was 63% at 2.36 μm. A record Johnson-noise-limited detectivity of $9.0 \times 10^{10}\mathrm{cmHz}^{1/2}/\mathrm{W}$ was achieved at 290K, with 50% cutoff wavelength of the photodiode at 2.57μm.

3.2 Principles of AlGaAsSb/InGaAsSb heterojunction photodiodes

Fig. 3.1 illustrates the band diagram of the AlGaAsSb/InGaAsSb heterojunction photodiode structure at room temperature and 1.0V reverse bias voltage. The device consisted of an n-type (2×10^{18} cm^{-3}) 0.05-μm-thick GaSb contact layer, a 0.5 μm $Al_{0.25}Ga_{0.75}As_{0.03}Sb_{0.97}$ wide-gap n-type layer (5×10^{17} cm^{-3}), a 2.5μm p-type (1×10^{16} cm^{-3}) unintentionally doped (n.i.d.) $In_{0.24}Ga_{0.76}As_{0.21}Sb_{0.79}$ absorption layer and a 1.0 μm heavily doped (1×10^{18} cm^{-3}) $In_{0.24}Ga_{0.76}As_{0.21}Sb_{0.79}$ for p-type contact. The material parameters and interpolation scheme of ternary and quaternary alloys are provided in Ref. [5]. All layers are lattice- matched to the GaSb substrate. Mid-infrared light from the front side of the photodetector passes through the wide-gap AlGaAsSb window and is absorbed by the InGaAsSb layers. The light intensity drops exponentially from the interface between AlGaAsSb and InGaAsSb, and the light absorption region overlaps with the depletion region in the InGaAsSb layer, which implies a high quantum efficiency of the photodiode. The length of the p-type InGaAsSb absorbing layer is much shorter than the diffusion length of electrons in it. Therefore, the photogenerated electrons in the quasi-neutral part of the InGaAsSb are able to diffuse effectively into the n-type region and contribute to the photocurrent. The valence band of the quaternary$Al_{0.25}Ga_{0.75}As_{0.03}Sb_{0.97}$ serves as a potential barrier, which dramatically reduces the holes diffusion from the n-side of the depletion region.[12] On the other hand, the heavily doped p-type InGaAsSb contact layer substantially decreases the minority carrier concentration in it. Thus, the dark current is further reduced by suppressing the electron diffusion through the p-side of the intrinsic InGaAsSb layer.[13]

3.3 InGaAsSb photodiodes fabrication and characterizations

The photodetector samples were grown on p-type GaSb (100) substrates by solid source MBE equipped with As and Sb crackers. The growth temperature was kept at 450 °C for InGaAsSb growth and 500 °C for the growth of AlGaAsSb. The V/III ratios and shutter sequences have been optimized based on comparison studies of the strength of photoluminescence (PL) for good material quality and smooth surface morphology. InGaAsSb bulk quaternary alloys were grown on GaSb(100) substrate before the growth of device structure. The as-grown InGaAsSb samples were first evaluated using a five crystal high-resolution X-ray diffractometer. The X-ray diffraction(XRD) results indicated that the InGaAsSb epilayer was lattice-matched to the GaSb substrate. Low-temperature photoluminescence was measured using the 514.5 nm line of the Ar-ion laser, a Bomem DA8 Fourier transform infrared (FTIR) spectrometer, and a liquid nitrogen-cooled InSb detector. Fig. 3.2 shows the photoluminescence of a typical 3 μm InGaAsSb bulk sample at 77K. As shown in the figure, clear and strong peak was observed at 2.2 mm with a full-width at half-maximum (FWHM) of 21meV, which indicated good crystalline quality of the InGaAsSb quaternary alloy. The band gap energy of the InGaAsSb was obtained from the peak wavelength of the PL spectrum, and together with the lattice constant from the XRD measurements, compositions of In(24%) and As(21%) in the InGaAsSb quaternary alloy can be determined.[5]

Photodetectors were fabricated by using wet chemical etching and a standard photo lithographic process. The device mesa was defined by etching down to the $In_{0.24}Ga_{0.76}As_{0.21}Sb_{0.79}$ p-type contact layer using a tartaric/phosphoric acid-based solution. Au/Ti layers were evaporated on top of the mesas and on the p-contact layer in a liftoff process to form ohmic contacts. The mesa has a rectangular shape (320μm × 140μm), with a rectangular

window (160μm × 140μm) on top of it. No passivation or antireflection dielectric coating was applied. Current–voltage (I–V) characteristics under different temperatures were measured by a HP4145B semiconductor parameter analyzer and a MMR cryogenic system. Capacitance–voltage(C–V) characteristics were measured using a Fluke PM6306 impedance analyzer with a four- point contacting scheme. Spectral responsivity measurements were carried out with a Bomem DA8FTIR spectrometer with a CaF_2 beam splitter, a blackbody source maintained at 1000K, and an Ithaco1211current preamplifier. The spectral responsivity curve of the photodetectors was determined by using an InSb photodetector with a precisely calibrated optical area and spectral response curve.

Fig. 3.3 shows the current–voltage characteristics of a typical photodiode at room temperatures under dark condition. The room temperature dark current of the device was measured to be 1.8 μA at reverse bias of 1.0V. This corresponded to a current density of 4.0mA/cm^2. The inset shows the I–V curve in the linear scale. As shown in the figure, the dark current increased gradually with the reverse bias voltage and a breakdown as high as 32Vwas observed. Capacitance–voltage characteristics of the photodiodes were measured at room temperature carried out at a test frequency of 100 kHz and oscillation level of 100 meV with bias voltages below 2.0 V.[14] The net doping concentration ($N_A - N_D$) of the intrinsic InGaAsSb layer was extracted by linearly fitting the capacitance versus bias voltage (C^{-2}–V) curve. The resulting residual carrier concentration of the InGaAsSb depletion region is in the range (8–10) × 10^{15} cm^{-3}.

Fig. 3.4 shows the spectral photoresponse curves at room temperature. The measurements were performed under zero bias with the photodiodes illuminated from the front side at normal

incidence. The device exhibits photoresponse up to 2.8 μm at room temperature. The 50% cutoff wavelength of the spectral responsecurve is 2.57 μm, which is consistent with the photoluminescence result of the InGaAsSb bulk material. The short wavelength cutoff at about1.3 μm is due to the energy bandgap of the AlGaAsSb window layer. The peak room temperature responsivity at the wavelength of 2.36 μm is1.16 A/W, which represents an external quantum efficiency of 63%. This also corresponds to an internal quantum efficiency of 90%, assuming a 30% surface reflectance from the uncoated device surface. The zero-bias resistance are a product (R_0A) was obtained from the slope of the *I–V* characteristic near zero bias.

The inset of Fig.3.5 illustrates R_0A plotted against 1000/T for the photodiode. As shown in the inset, R_0A is 90 Ω cm^2 at 290K and 1.1×10^5 Ω cm^2at 190K. The activation energy of about 310 meV can be extracted from the slope of the curve near room temperature. By taking into consideration that the energy gap of InGaAsSb varies with temperature.[15] the theoretical prediction of the activation energy for the generation–recombination (G–R) limited case is calculated to be 296 meV. This indicates that the dark current is dominated by G–R mechanism near room temperature up to 340 K. The ideality factor of the photodiode is calculated to be 1.9. It also confirms that the diffusion components of the dark current are effectively suppressed by the n-type AlGaAsSb barrier and the heavily doped p-type InGaAsSb at the both ends of the intrinsic InGaAsSb layer. At temperature lower than190K, the saturation of R_0A is due to surface leakage through the mesa edge. The Johnson-noise-limited detectivity (D*) for the AlGaAsSb/InGaAsSb photodiodes at a specific temperature can be evaluated, given the zero-bias resistance and photoresponsivity.[12] The resulting peak Johnson-noise-limited detectivity of the photodetector is 9.0×10^{10}cm $Hz^{1/2}$/W at 290K. To our knowledge, this is the highest at this

temperature Johnson-noise-limited detectivity reported so far for InGaAsSb photodiodes grown by MBE. Fig.3.5 illustrates the temperature dependence of the peak Johnson- noise-limited detectivity for the InGaAsSb photodiodes.

3.4 Summary and Conclusion

AlGaAsSb/InGaAsSb heterojunction photodiodes lattice-matched to GaSb substrates grown by solid source molecular beam epitaxy have been demonstrated. High-resolution XRD and low-temperature PL indicated good material quality of the InGaAsSb layer lattice-matched to GaSb. The heterojunction photodiodes exhibited low dark current of 4mA/cm^2 (1V) and a breakdown voltage of 32Vat room temperature. The room temperature peak external quantum efficiency of the photodiode was 63%. A record Johnson-noise-limited detectivity of 9.0 × 10^{10}cm Hz$^{1/2}$/W was achieved at 290K. Room temperature spectral response was obtained with the 50% cutoff wavelength that 2.57 μm. The dark current of the photodetector is dominated by the generation–recombination (G–R) mechanism at temperatures up to 340K. Data reported here demonstrated that InGaAsSb photodiode is a very promising candidate for various applications in the wavelength range 2.0–3.0 μm, such as molecular spectroscopy, blood glucose sensing and laser radar systems.

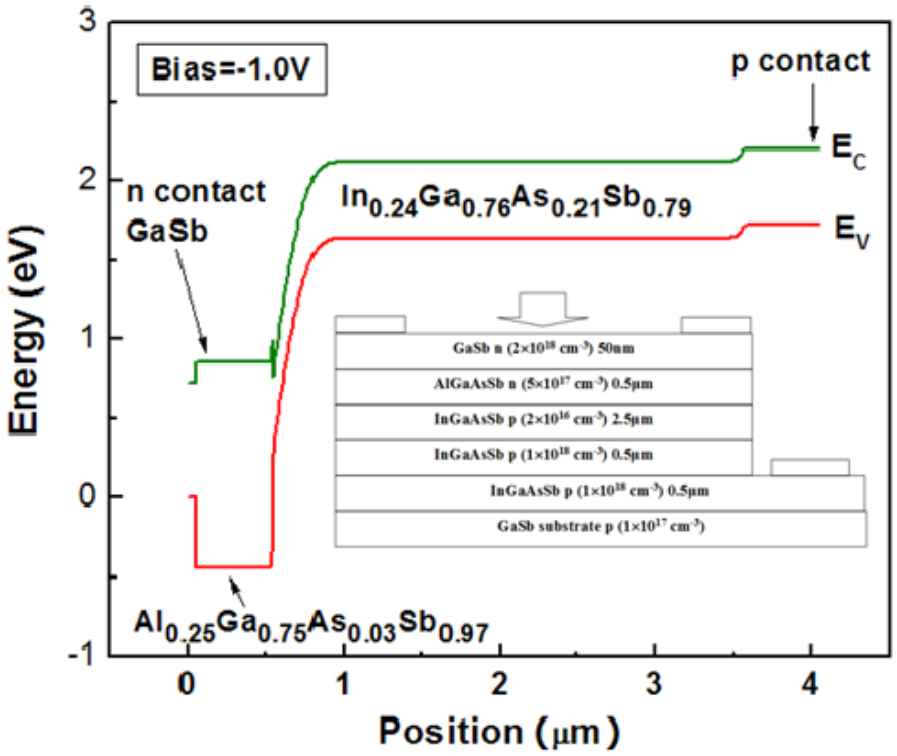

FIG. 3.1 The energy band diagram of the AlGaAsSb/InGaAsSb photodiode at room temperature and reverse bias voltage of 1.0V. The inset shows the cross-sectional structure of the photodiode.

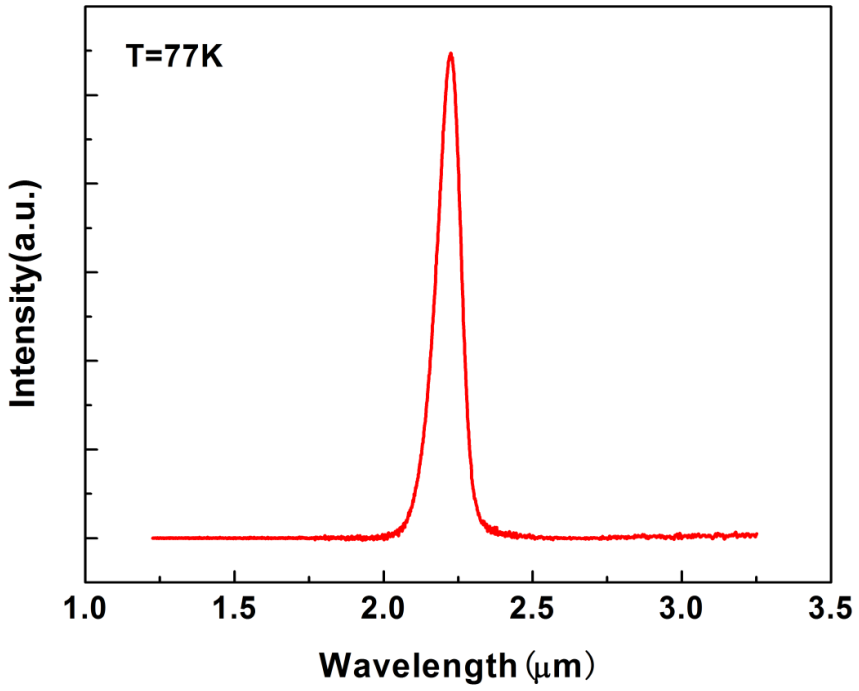

FIG. 3.2 Typical 77K photoluminescence for bulk 3-μm-thick lattice-matched InGaAsSb grown on GaSb substrate.

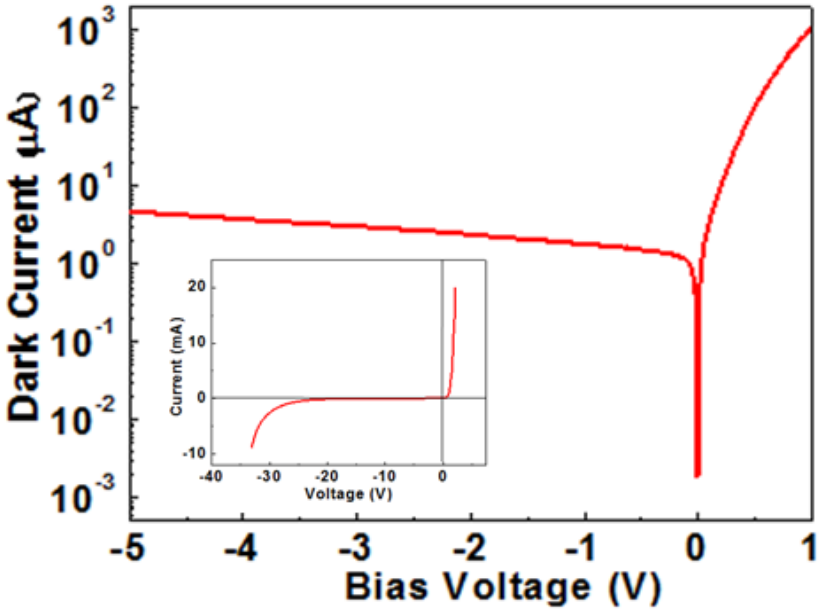

FIG. 3.3 *I–V* characteristics of the AlGaAsSb/InGaAsSb photodiode under dark condition at room temperature. The area of the device mesa is 320 μm × 140 μm. Inset shows the *I–V* characteristic in linear scale. Reverse break down voltage is about 32V.

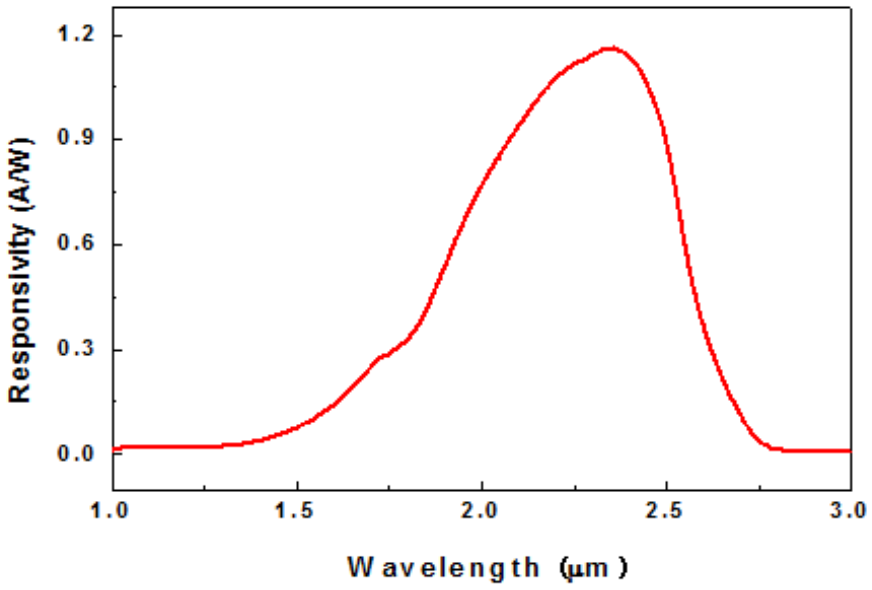

FIG.3. 4. Spectral response of the AlGaAsSb/InGaAsSb photodiode at 290K and zero bias. The 50% cutoff wavelength is at 2.57 μm. The peak external quantum efficiency is 63% at 2.36 μm.

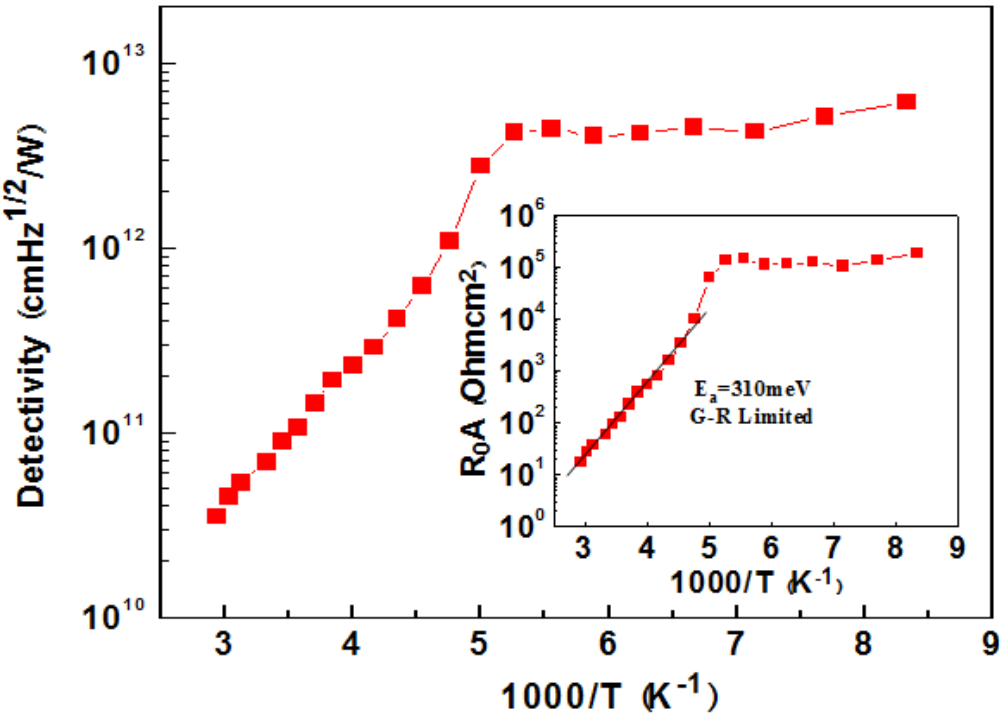

FIG. 3.5. Temperature dependence of the peak Johnson-noise-limited detectivity (D*) for a typical AlGaAsSb/InGaAsSb photodiode. Inset shows the temperature dependence of the resistance are a product (R_0A). Above the crossover temperature of 190K, R_0A is dominated by the *G–R* mechanism with an activation energy E_a = 310 meV. Below 190K, the R_0A is dominated by the surface leakage.

References

1. J.D. Phillips, K. Moazzami, J. Kim, D.D. Edwall, D.L. Lee, J.M. Arias, Appl. Phys. Lett. 83 (2003) 3701.

2. R.Schoolar, E. Tenescu, Proc. SPIE686 (1986) 2.

3. R.Sidhu, N.Duan, J.C. Campbell, A.L. HolmesJr., IEEE Photonics Technol. Lett. 17(2005) 2715.

4. M.Wada, H. Hosomatsu, Appl. Phys. Lett.64 (10) (1994) 1265.

5. I. Vurgaftman, J.R. Meyer, L.R. Ram-Mohan, J. Appl. Phys.89 (2001) 5815.

6. A.K. Srivastava, J.C. DeWinter, C.Caneau, M.A. Pollack, J.L. Zyskind, Appl. Phys. Lett. 48 (1986) 903.

7. C.A. Wang, H.K. Choi, G.W. Charache, IEE Proc. - Optoelectron. 147(2000) 193.

8. B.L. Carter, E. Shaw, J.T. Olesberg, W.K. Chan, T.C. Hansenberg, M.E. Flatte, Electron. Lett. 36 (2000) 1301.

9. C. Lin, Y.L. Zheng, A.Z. Li, J.Crystal Growth 227 (2001) 605.

10. J.G. Cederberg, M.J. Hafich, R.M. Biefeld, M. Palmisiano, J. Crystal Growth 248 (2003) 289.

11. M.H.M. Reddy, J.T. Olesberg, C. Cao, J.P. Prineas, Semicond. Sci. Technol. 21 (2006) 267.

12. A. Rakovska, V. Berger, X. Marcadet, B. Vinter, G. Glastre, T. Oksenhendler, D. Kaplan, Appl. Phys. Lett. 77 (2000) 397.

13. S.M.Sze, Physics of Semiconductor Devices, Wiley-Interscience, NewYork, 1981.

14. A. Hood, D. Hoffman, Y. Wei, F. Fuchs, M.Razeghi, Appl. Phys. Lett.88 (2006) 0521121.

15. G. Marre, B. Vinter, V. Berger, Semicond. Sci. Technol. 18 (2003) 284.

Chapter 4

Phosphor-free 1.3μm InAlGaAs multiple-quantum-well (MQW) lasers on InP (100)

4.1 Introduction

Semiconductor lasers operating at a wavelength of 1.3 μm are of great interest for applications in the field of optical communication systems. 1.3 μm InGaAsP/InP lasers are used extensively in current communication systems. However, thermoelectric coolers are required to keep the laser operating temperature constant because, if uncooled, 1.3–1.55 μm InGaAsP/InP lasers exhibit a low characteristic temperature T_0(typically 60–65 K) and large variations in differential-quantum efficiency (more than 1 dB) over the working temperature range from 25 to 85°C.[1] These uncooled InGaAsP lasers are too temperature sensitive to meet the strict requirements for optical communication systems.[2,3] While thermoelectric cooler improves the temperature stability, it adds to the cost of the laser transmitter and the issues about long-term reliability at the same time.[1]

As a result, 1.3 μm high-temperature-stability semiconductor lasers become a key technology for the development of practical low-cost, high-performance optical communication systems. One of the leading contenders for high performance 1.3 μm lasers is the InAlGaAs based material system on an InP substrate. This material system is targeted to improve the temperature stability of the laser performances by exploring the advantages of their larger conduction band offsets compared to the conventional InGaAsP/InP system. Figure 4.1 shows the schematic band alignment for the basic materials lattice matched to InP substrate. The InAlGaAs material system matched on an InP substrate has a larger wavelength range (from 0.75 eV for $In_{0.53}Al_{0.47}As$ to 1.45 eV for $In_{0.52}Al_{0.48}As$) than that of the matched InGaAsP system (from 0.75 eV for $In_{0.53}Al_{0.47}As$ to 1.34 eV for InP). More importantly, the matched InAlGaAs material system shows a much larger conduction offset (ΔE_C = 0.75 ΔE_g) than that of matched

InGaAsP (ΔE_C = 0.40 ΔE_g), which is the key in obtaining quantum-well (QW) lasers with higher T_0 than conventional InGaAsP QW lasers.[4,5]

High-quality InAlGaAs lasers are usually grown by metal-organic chemical-vapor deposition,[1,6] chemical beam epitaxy,[7] or gas-source molecular-beam epitaxy.[7] However, the high toxicity of hydride gas sources, such as arsine (AsH_3) and phosphine (PH_3) used in these growth tools, and the expensive gas handling and safety systems motivate the growing of high-quality InAlGaAs lasers by solid-source molecular-beam epitaxy (SSMBE). However, even in a SSMBE system, a solid-source phosphorus cracker source requires an extreme effort to safely maintain the MBE system due to the high flammability of white phosphorus. As a result, in this chapter, 1.3 μm InAlGaAs strain-compensated-multiple-quantum well (SCMQW) lasers without any phosphor containing layers in epitaxial structures were designed and developed. We also investigated the growth of InAlGaAs material on InP by SSMBE and demonstrated that high quality 1.3μm InAlGaAs lasers can be achieved by SSMBE without a P_2 cracking cell.

4.2 Experiments

All the samples were grown in a GEN-II solid-source MBE system. The growth structures were characterized by reflection high-energy electron diffraction, high-resolution x-ray diffraction (HRXRD), and room-temperature photoluminescence (PL). HRXRD measurements were carried out with a Philips five-crystal x-ray diffractometer using the (400) reflection. Room-temperature PL measurements were performed using a 514.5 nm Ar^+ laser, a Bomem DA8 Fourier-transform-infrared spectrometer, and an InGaAs detector. InAlGaAs broad-area lasers were fabricated by using AuZn and AuGe/Ni metallization for the p- and n-type con- tacts. The laser performances were characterized by lightcurrent (L-I) and wavelength measurements at various heat-sink temperatures.

4.3 Results and Discussions

4.3.1 Growth of InAlGaAs Matched Layers

In the laser structure shown in Fig. 4.2, InAl(Ga)As layers matched to the InP substrate are very important for the whole laser structures because they serve as part of the bottom cladding layers (n-$In_{0.52}Al_{0.48}As$), both bottom and top waveguide layers (undoped $In_{0.52}Al_{0.32}Ga_{0.16}As$), and the top cladding layer (n-$In_{0.52}Al_{0.48}As$). Calculations and experiments about the band-gap energy of matched InAlGaAs were made as early as 1982.[9]

However, it still requires an extreme effort to achieve high-quality InAlGaAs materials. Moreover, the band-gap energy of lattice-matched InAlGaAs layers in practical growth runs can deviate significantly from the calculated result due to many phenomena occurring in real growth, such as spontaneous alloy ordering and phase separation.[10−13] In our experiments, we found that the growth temperature was very critical to achieving high-quality matched InAlGaAs layers with a band-gap energy corresponding to that of random alloys. When the growth temperature was between 485 and 520 °C, spontaneously ordered alloys with vertical InAlGaAs superlattice (SL) structure with well-defined periods of 7–10 nm was formed during the growth of InAlGaAs bulk layers. Figure 4.3 shows the typical XRD result of a matched $In_{0.52}Al_{0.48}As$ on InP (100) substrate at 490 °C by SSMBE.

The major InAlAs (400) peak was merged with the InP (400) substrate peak, indicating that the average composition of the InAlAs bulk layer was $In_{0.52}Al_{0.48}As$. However, in contrast to those InAlAs bulk layers grown under an optimized temperature, a pair of InAlAs satellite peaks are located symmetrically on both sides of InP (400), indicating the existence of a well defined spontaneous SL with period of 7.4 nm inside the bulk $In_{0.52}Al_{0.48}As$. This is the first

observation of a well defined spontaneous vertical InAlGaAs SL along the growth direction even though some other spontaneous structures in InAlGaAs, such as atomic ordering and lateral composition modulation, were reported previously.[11−13]

Room-temperature PL was measured to compare the band-gap energies of the $In_{0.52}Al_{0.48}As$ samples with and without spontaneous SL. As shown in Fig. 4.4, a reduction of band-gap energy as large as 300 meV was observed in the spontaneously ordered $In_{0.52}Al_{0.48}As$ samples with SL as compared to the $In_{0.52}Al_{0.48}As$ bulk samples without ordering, corresponding to a large redshift of PL peak wavelength from 0.856 to 1.06 μm. The PL peak of the spontaneously ordered InAlAs with SL [full width at half maximum (FWHM) ~126 meV] was much broader than that of the InAlAs [FWHM ~ 65 meV] random alloy, as expected. Therefore, the growth of matched $In_{0.52}Al_{0.48}As$ cladding layers and InAlGaAs waveguide layers should be carefully optimized. In further experiments, we found that the undesirable spontaneous ordering can be avoided by increasing the growth temperature higher than 530 °C.

4.3.2 Growth of InAlGaAs Multiple-Quantum-Well (MQW)

In our 1.3 μm InAlGaAs MQW laser structures shown in Fig. 4.2, both barrier and well layers in the QW active region were InAlGaAs layers with tensile strain (~ 0.3%) and compressive strain (~1%), respectively. Strain compensation was introduced in the InAlGaAs MQW active region to obtain larger carrier confinement and take advantage of the strain effects. The 1.3 μm InAlGaAs/InAlGaAs SCMQW demonstrated higher emission efficiency and narrower PL peak in comparison with lattice-matched InAlGaAs/InAlGaAs MQW. As shown in Fig. 4.5, the PL intensity was increased by 100% and the PL peak was narrowed by 80% by introducing strain compensation in InAlGaAs MQW.

4.3.3 Performances of InAlGaAs SCMQW Lasers

Figure 4.2 shows the schematic structure of our InAlGaAs/InAlGaAs SCMQW lasers including three $In_{0.68}Al_{0.11}Ga_{0.21}As/In_{0.48}Al_{0.37}Ga_{0.15}As$ QWs. The InP (100) substrate also acted as part of the n-cladding layer, which reduced the growth time of the n-InAlAs layer. All the InAlGaAs layers were grown at 530 °C to avoid the spontaneous alloy ordering, while the InGaAs cap layer was grown at 460 °C. Broad-area lasers were fabricated by using AuZn and AuGe/Ni metallization for the p- and n-type contacts, respectively. Figure 4.6 shows the *L-I* curve and lasing spectrum of a 1.2 mm × 120μm InAlGaAs MQW laser. The pulsed threshold-current density at room temperature was as low as 690 A/cm^2 and the lasing wavelength was 1.314 μm, which indicates that the InAlGaAs SCMQW laser grown by SSMBE can be a promising candidate for high-performance 1.3 μm semiconductor lasers. Figure 4.7 shows a T_0 as high as 80 K for these SSMBE-grown InAlGaAs MQW lasers, which is much improved compared to conventional InGaAsP QW lasers.

4.4 Summary and Conclusion

Substrate temperature was found to be a very critical parameter during SSMBE growth of InAlGaAs on InP. When the temperature was between 485 and 520 °C, spontaneous ordering with SL was formed during the growth of InAlGaAs layers lattice matched to InP. This corresponds to a redshift of band-gap energy as large as 300 meV in the spontaneously ordered $In_{0.52}Al_{0.48}As$ layer. By optimizing the growth temperature and the multiple-quantum-well **(**MQW) structure design, high performance 1.3 μm InAlGaAs lasers without any phosphor containing layer in the epitaxial structures were achieved by SSMBE. Threshold-current density as low as 690 A/cm^2 and T_0 as high as 80K were achieved for the InAlGaAs lasers emitting at 1310 nm.

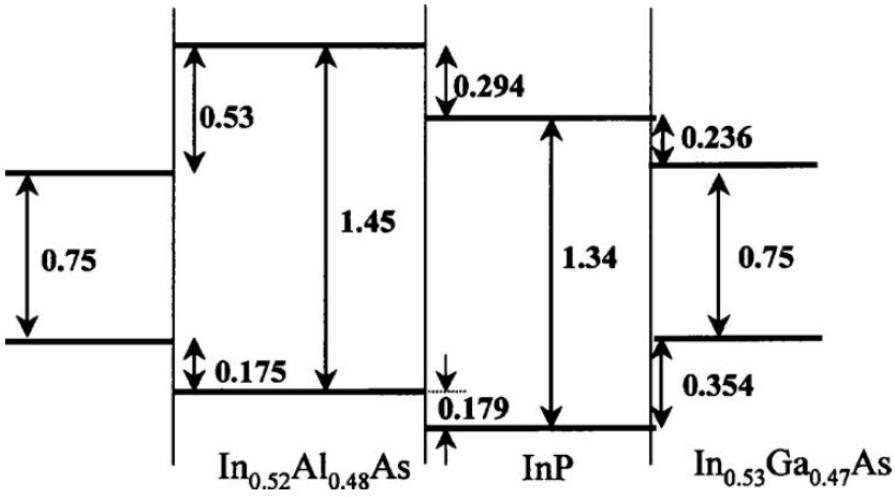

FIG.4.1 Band offsets between the InAlGaAs materials lattice matched on InP substrate.

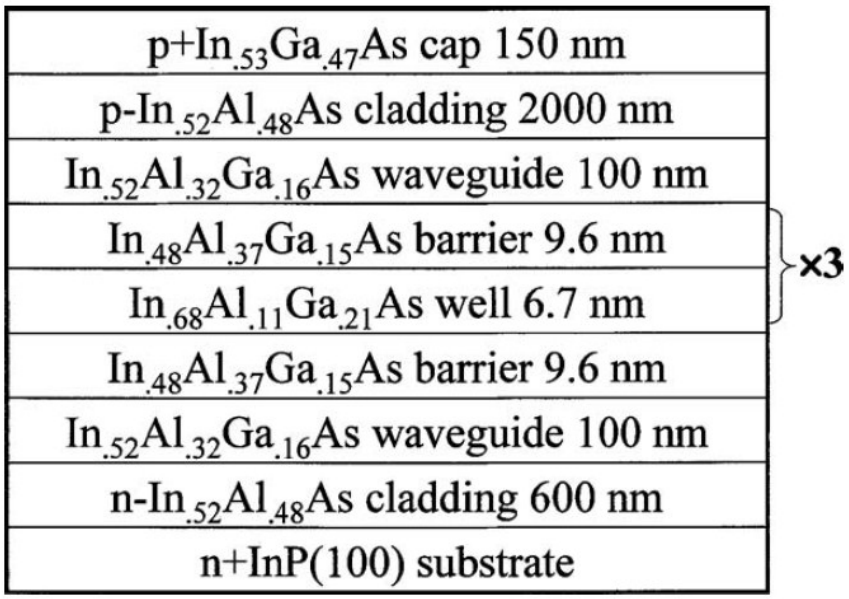

FIG.4.2 Schematic structure of 1.3 μm InAlGaAs strain-compensated multiple-quantum-well (SCMQW) laser.

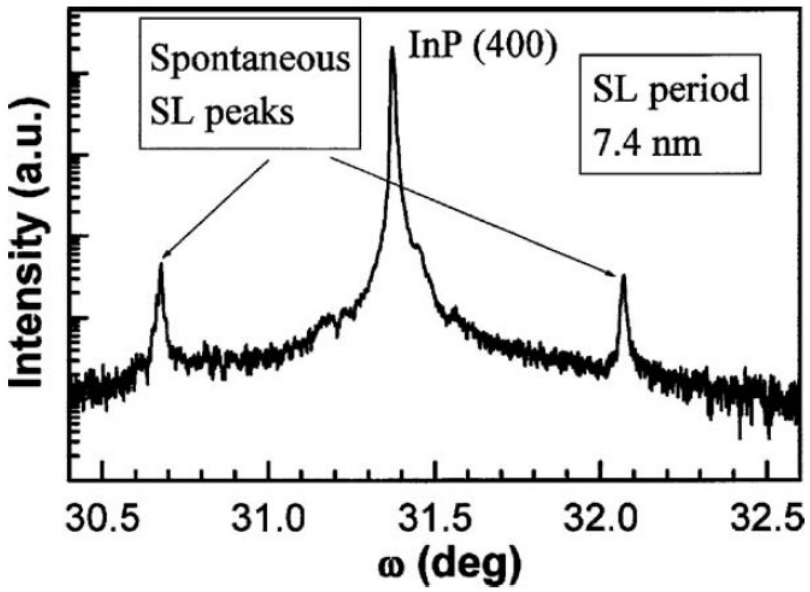

FIG.4.3 XRD result of ordered $In_{0.52}Al_{0.48}As$ on InP (100) grown at 490 °C with spontaneous ordered superlattices.

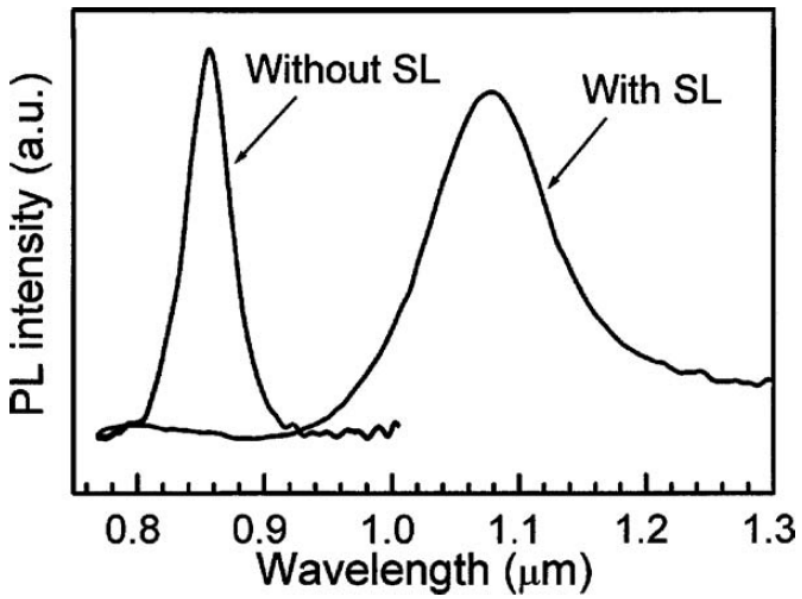

FIG.4.4 Photoluminescence spectra of $In_{0.52}Al_{0.48}As$ layers with and without spontaneous superlattices.

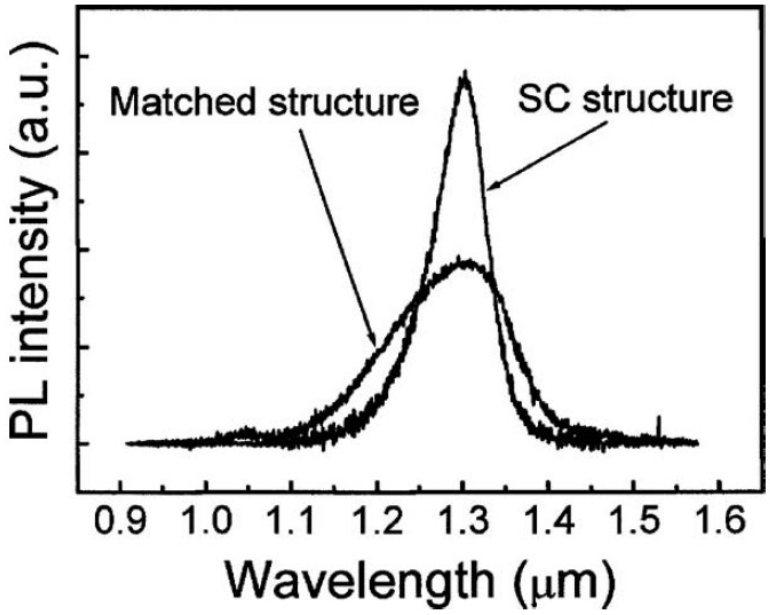

FIG.4.5 Photoluminescence spectra of InAlGaAs MQWs with strain compensated and lattice-matched well/barrier layers.

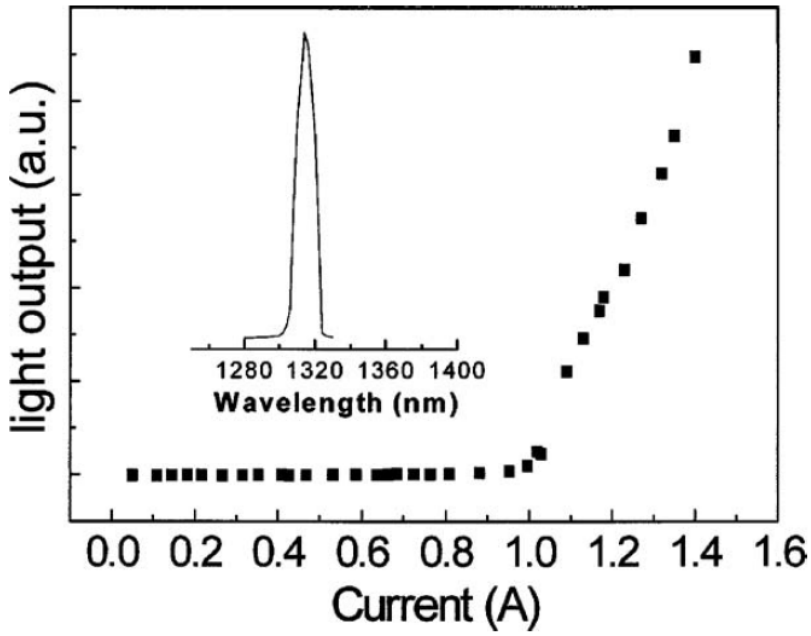

FIG.4.6 L-I curve and lasing wavelength of room-temperature InAlGaAs SCMQW lasers (1.2 mm×120μm) under pulsed condition (1μs,1 kHz).

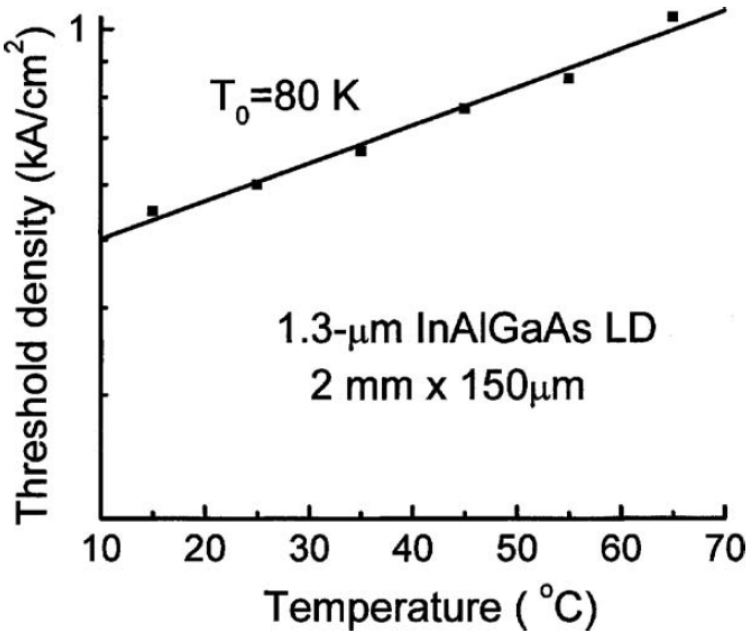

FIG.4.7 Dependence of threshold-current density of InAlGaAs SCMQW lasers on operating temperature.

References

1. C. E. Zah et al., IEEE J. Quantum Electron. 30, 511 (1994).

2. Bellcore, Report No. TA-TSY-000983 1990 (unpublished).

3. C. E. Zah et al., Electron. Lett. 27, 1414 (1991).

4. M. Kondow, K. Uomi, A. Niwa, T. Kitatani, S. Watahiki, and Y. Yazawa,Jpn. J. Appl. Phys., Part 1 35, 1273 (1996).

5. M. Kondow, T. Kitatani, S. Nakatsuka, M. C. Larson, K. Nakahara, Y.Yazawa, M. Okai, and K. Uomi, IEEE J. Sel. Top. Quantum Electron. 3,719 (1997).

6. M. Kito, N. Nobuyuki, M. Ishino, and Y. Matsui, IEEE J. Quantum Electron.30, 38 (1996).

7. S. Husser, C. S. Harder, H. P. Meier, and W. Walter, Appl. Phys. Lett. 62,663 (1993).

8. G. J. Shian, C. P. Chao, P. E. Burrows, and S. R. Forrest, Appl. Phys. Lett.65, 892 (1994).

9. D. Olego, T. Y. Chang, E. Silberg, E. A. Caridi, and A. Pinczuk, Appl.Phys. Lett. 41, 476 (1982).

10. T. S. Kuan, T. F. Kuech, W. I. Wang, and E. L. Wilkie, Phys. Rev. Lett.54, 201 (1985); T. S. Kuan, W. I. Wang, and E. L. Wilkie, Appl. Phys.Lett. 51, 51 (1987).

11. W. S. Han, B. Lee, J. H. Baek, J. H. Lee, B. S. Jung, E. H. Lee, and O.Byungsung, Appl. Phys. Lett. 72, 1905 (1998).

12. Y. Zhang and A. Mascarenhas, Phys. Rev. B 57, 12245 (1998).

13. R. L. Forrest and J. Kulik, J. Mater. Res. 15, 45 (2000).

Chapter 5

InGaAsNSb/GaAs quantum wells on GaAs (411) substrates by MBE

5.1 Introduction

Long-wavelength (1.3–1.55 μm) GaAs-based lasers containing InGaAsN/GaAs quantum wells (QWs) on GaAs substrates have attracted much attention in recent years.[1−3]. The potential advantages of the long-wavelength GaAs-based edge emitting lasers and vertical-cavity surface emitting lasers (VCSELs) over the InP-based counterpart include ease of manufacture and low cost due to the matured GaAs material and fabrication technologies, availability of lattice-matched distributed bragg reflector mirrors with high reflectance and thermal conductivity, and reduced temperature sensitivity due to the large conduction band offset between the GaAs barrier and InGaAsN well.[4]

High-quality InGaAsN/GaAs QW active region is one of the keys to achieve high performance GaAs-based vertical-cavity surface-emitting lasers (VCSELs) and, as a result, intensive effort has been made to improve the quality of InGaAsN/GaAs QWs. Recently, it was proposed and demonstrated by Yang et al[5−7]that adding a small amount of Sb during the growth of InGaAsN QWs, which results in Sb surfactant effect and InGaAsNSb quinternary compound, could significantly improve the structural and optical qualities of the InGaAsN/GaAs QWs in the 1.3–1.55 μm range. As a result, the device performances of the long-wavelength laser diodes including both VCSELs and edge emitters were improved greatly by using InGaAsNSb/GaAs QWs .[3,7−9]

However, all the previous InGaAsN (Sb) /GaAs QWs have been grown on conventional GaAs (100) substrate. In this chapter, we propose to improve the optical qualities of the InGaAsNSb/GaAs QWs by growing them on GaAs (411)A rather than on GaAs (100). Remarkable enhancement of the photoluminescence (PL) efficiency was observed in the 1.3 μm

InGaAsNSb/GaAs single quantum well (SQW) samples grown on GaAs (411)A as compared to those grown on GaAs (100). We also found that the optimal growth temperature for (411)A is 30° higher than that for (100).

The motivation for selecting (411) was due to the observation that (411) evolves naturally as a stable facet during molecular beam epitaxy (MBE) crystal growth,[10] as shown in Fig. 5.1. This experimental discovery cannot be predicted by any *ab initio* calculations. In fact, to date, the choice of a particular crystal orientation to achieve superior material quality remains empirical.

Figure 5.2 shows the atomic arrangement of GaAs (411)A surface, which is formed by tilting GaAs (100) toward (111)A by 19.5°. The GaAs (411)A surface.[11−13] is composed of both double-dangling As bond sites and single-dangling Ga bond sites, resulting in (100) terraces and (111)A steps, as highlighted by the bold line in Fig. 5.2.

In this chapter, data are presented to show the advantages of (411) orientation for the growth of InGaAsNSb/GaAs QWs. The optical quality of the InGaAsSbN/GaAs QWs were improved considerably by growing on the GaAs (411)A orientation.

5.2 Experiments

All the InGaAsNSb/GaAs QW samples were grown by a Varian Gen-II solid-source MBE system equipped with As and Sb crackers. Ultrahigh purity $N_2$was injected through a radio-frequency plasma cell (SVT Associates) to generate reactive atomic nitrogen. Prior to the InGaAsSbN/GaAs QW growth on GaAs (411)A, a number of InGaAsSb/GaAs and InGaAsNSb/GaAs multiple quantum well samples were grown on GaAs (100) to calibrate the compositions in QWs using x-ray diffraction and secondary ion mass spectrometry methods and to optimize the growth conditions for InGaAsSbN/GaAs QWs on GaAs (100), as detailed in Ref.6. Under the optimum growth conditions for GaAs (100), 1.3 μm InGaAsSbN/GaAs SQW samples on GaAs (411)A were grown with one piece of GaAs (100) loaded in the same molybdenum block as reference. The optical properties of the InGaAsNSb/GaAs SQW samples on GaAs (411)A and (100) were then compared by room-temperature (RT) PL measurements, which were performed using a 514.5 nm argon ion laser and a Bomem DA8 Fourier transform infrared spectrometer.

5.3 Results and Discussions

During MBE growth we observed that GaAs (411)A showed no reflection high energy electron diffraction (RHEED) oscillations, due to the out of the phase scattering factor of the electron beam, whereas the lack of RHEED oscillations on (211), (311), and(511)$^{13-16}$ is due to the relative short terrace width compared to the diffusion length of the surface adatom species.

PL measurements (RT) with a liquid-nitrogen-cooled InGaAs detector were used to characterize the 1.3 μm $In_{0.3}GaAsN_{0.008}Sb$ (6.7 nm)/GaAs SQWs on GaAs (411)A and (100) grown side by side. One striking feature of the InGaAsNSb/GaAs SQW samples on GaAs (411)A is its very high PL peak intensity, which is four times stronger than that of GaAs (100), as shown in Fig. 5.3. The full width at half maximum value of the PL peak on GaAs (411)A (40 meV) is 17% smaller than that on GaAs (100) (48 meV). Note that these InGaAsNSb SQW samples on GaAs (411)A were grown at 450 °C, the optimum growth temperature for GaAs(100). In the experiments, the optimum growth temperature Was 450 °C for InGaAsNSb/GaAs QWs on GaAs (100), (311), and (511) substrates, based on RHEED observations,whereas on GaAs (411)A it was 480 °C, the temperature at which the RHEED for (100) InGaAsNSb/GaAs QW collapsed into spotty and rough patterns.

Similar phenomena were observed in the growth of InAs quantum dots (QDs) on GaAs (411)A and GaAs (100), both with a 1 μm GaAs buffer layer. Figure 5.4 shows the morphology of InAs QDs on GaAs (411)A and GaAs (100) by atomic force microscopy (AFM). The (411) surface is clearly smoother, with flat regions on the order of 1 μm as compared to a few hundred to a thousand angstroms for (100).

In order to explain that the optimum growth temperature of GaAs (411)A was 30 °C higher than that of other orientations such as (100), (311), and (511), a model based on the self-assembling of the local rough surfaces of (311) and(511) domains to the "global" smooth surface on the (411)A is proposed. From Fig. 5.2, it can be seen that (411) is not a fundamental surface. Rather, it is a combination of the fundamental (311) and (511) surfaces,[14] as shown in Fig. 5.5(a). The (411) surface consists of local (311) and (511) domains and is rough with wrinkles on the order of hundreds of angstroms at 450 °C, reflected by the rough RHEED patterns. The roughness and wrinkles were completely annealed out at 480 °C, which corresponds to a thermal energy of 65 meV. This means that a thermal energy of 65 meV is required to overcome the surface diffusion barrier for adatom species to reach the global smooth surface on (411)A, as shown in Fig.5.5(b). By definition, there is only one global smooth surface. The global smooth (411)A surface is the unique lowest energy state of the system and exhibits extreme surface smoothness on a scale of microns, as opposed to the infinite number of rough surfaces which correspond to multiple higher energy states.

We have recently grown InGaAsNSb(411) SQW lasers (7 nm SQW, 100 nm GaAs inner cladding layer, and 1.5 μm $Al_{0.35}Ga_{0.65}As$ outer cladding layer) with threshold current density of 283 A/cm^2, the lowest ever achieved for the quinternary InGaAsNSb material system. The light-current (*L-I*) curve and lasing spectrum is shown in Fig. 5.6. This further demonstrates the superior interface and optical qualities of InGaAsNSb(411).

5.4 Summary and Conclusion

A novel promising quinternary material InGaAsNSb and InGaAsNSb/GaAs QW for 1.3 μm fiber optic applications have been grown on GaAs (411)A substrates by molecular beam epitaxy for the first time.

InGaAsNSb/GaAs QWs on GaAs (411)A exhibited remarkably enhanced PL efficiency compared with the same structures on conventional GaAs (100) substrates grown side by side, under the optimized growth temperature for (100) but not for (411). The experiments also revealed that the optimum growth temperature for (411)A is 480 °C, i.e., 30 °C higher than that for (100), (311), and (511) orientations (i.e.,450 °C). A model is proposed based on the self-assembling of local rough domains at the growth temperature of 480 °C on the (411)A, which corresponds to a 65 meV energy barrier for the local short terrace domains of (311) and (511) to overcome in order to reach the global smooth (411) surface. The 65 meV observed in the experiments is exceedingly difficult for any *ab initio* theoretical calculations to predict and indicated the importance of the empirical experimental approach presented in this chapter.

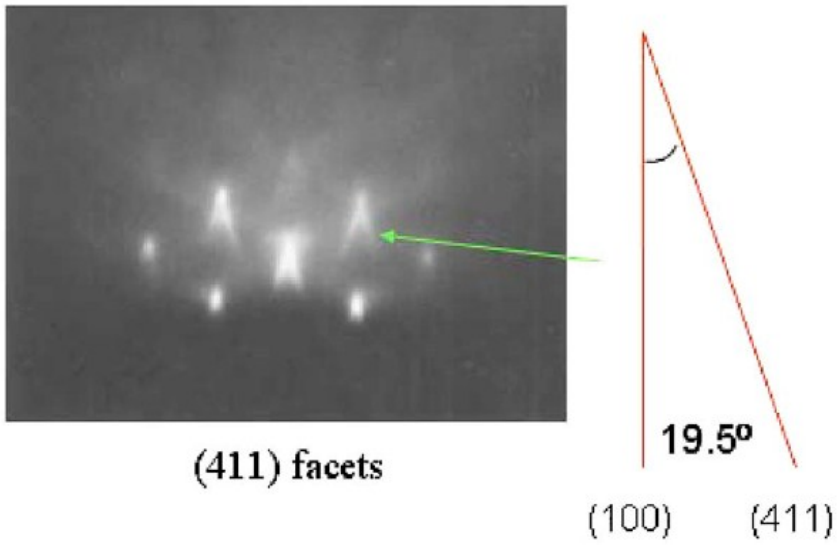

FIG. 5.1 (411) is a naturally stable surface for MBE growth, as clearly seen in the RHEED pattern.

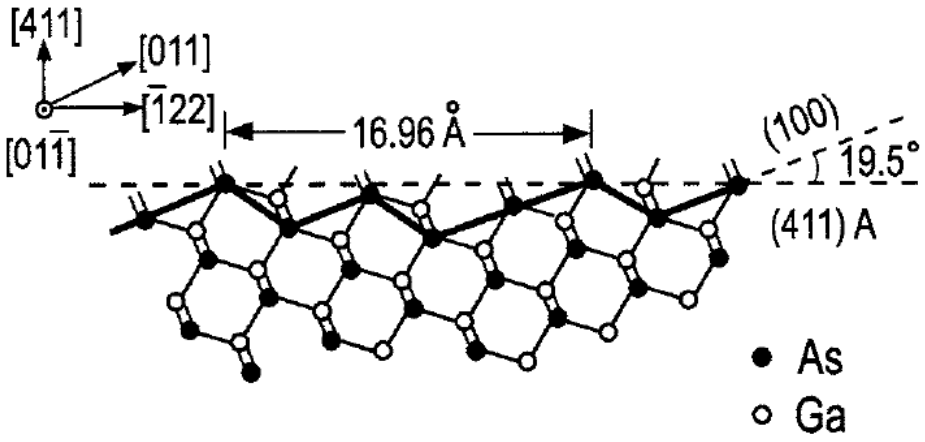

FIG. 5.2 Atomic arrangement of GaAs (411)A with surface terraces and steps highlighted by bold lines.

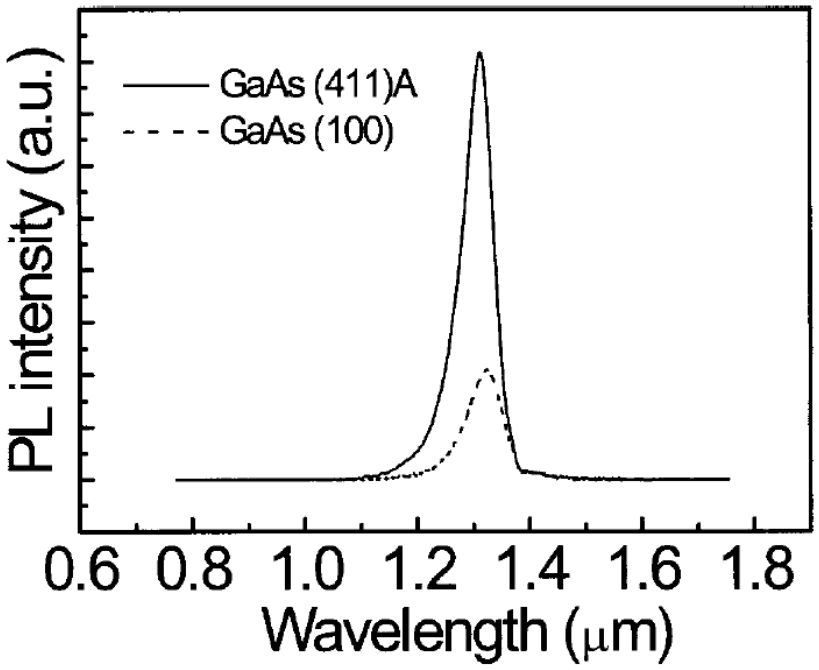

FIG. 5.3 PL spectra of the 1.3 μm InGaAsNSb/GaAs SQW samples on GaAs (411)A and GaAs (100) grown side by side.

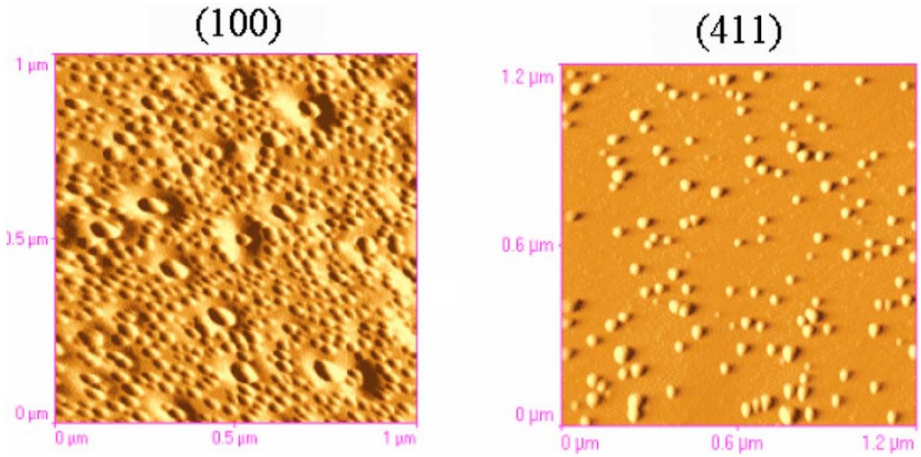

FIG. 5.4 AFM photos of InAs QDs on GaAs (411)A and GaAs (100). The (411) surface is clearly smoother, with flat regions on the order of 1 µm.

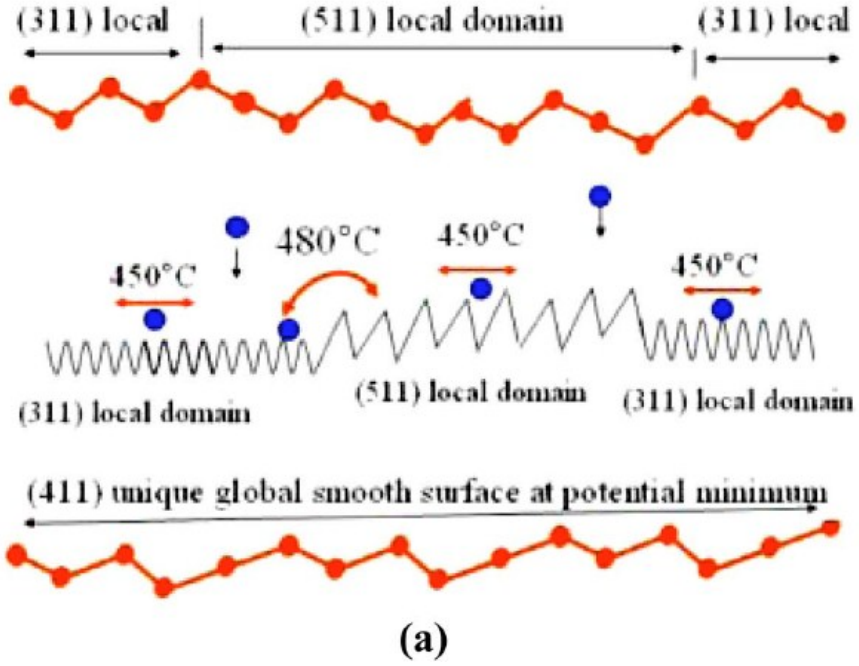

FIG. 5.5 (a) Diagram of self-assembling of local (311) and (511) domains on (411)A surface between the growth temperatures of 450 and 480 °C.

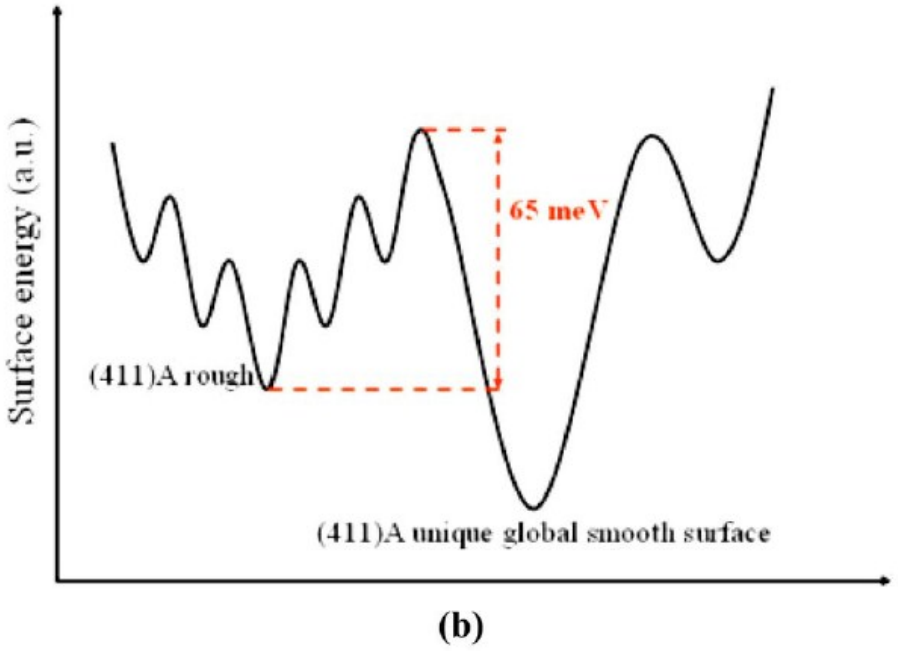

FIG. 5.5 (b) A thermal energy of 65 meV (480 °C) is required for surface adatom species to overcome the diffusion barrier to reach the unique global smooth surface on (411)A.

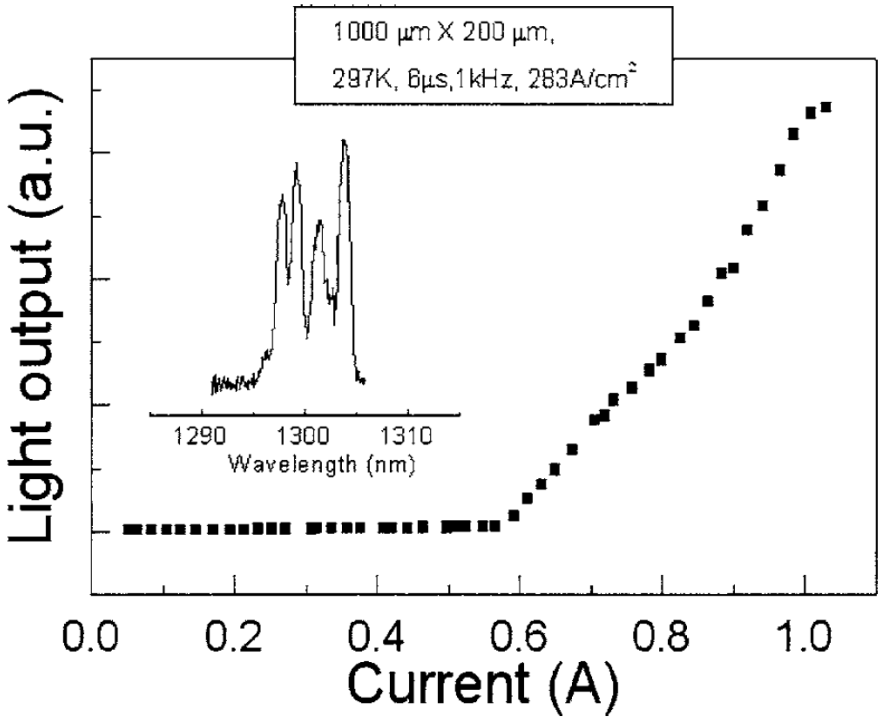

FIG. 5.6 *L-I* curve of an InGaAsNSb/GaAs SQW laser at room temperature.

References

1. M. C. Larson, M. Knodow, T. Kitatani, K. Nakahara, K. Tamura, H.Inoue, and K. Uomi, IEEE Photonics Technol. Lett. 10, 188 (1998).

2. W. Jackson et al., Electron. Lett. 37, 355 (2001).

3. M. A. Wistey, S. R. Bank, H. B. Yuen, L. L. Goddard, and J. S. Harris, J.Vac. Sci. Technol. B 22, 1562 (2004).

4. M. Kondow, T. Kitatani, S. Nakatsuka, M. C. Larson, K. Yazawa, and K.Uomi, IEEE J. Sel. Top. Quantum Electron. 3, 719 (1997).

5. X. Yang, M. J. Jurlovic, J. B. Heroux, and W. I. Wang, Appl. Phys. Lett.75, 178 (1999).

6. X. Yang, J. B. Heroux, L. F. Mei, and W. I. Wang, Appl. Phys. Lett. 78,4068 (2001).

7. X. Yang, J. B. Heroux, M. J. Jurkovic, and W. I. Wang, Appl. Phys. Lett.76, 795 (2000).

8. L. H. Li, V. Sallet, G. Patriache, L. Largeu, S. Bouchoule, L. Travers, andJ. C. Harmand, Appl. Phys. Lett. 83, 1298 (2003).

9. S. R. Bank, M. A. Wistey, L. L. Goddard, H. B. Yuen, V. Lordi, and J. S.Harris, IEEE J. Quantum Electron. 40, 656 (2004).

10. W. I. Wang, J. Vac. Sci. Technol. B 1, 574 (1983).

11. S. Shimomura, A. Wakejima, A. Adachi, Y. Okamoto, N. Sano, K.Murase, and S. Hiyamizu, Jpn. J. Appl. Phys., Part 2 32, L1728 _1993_.

12. S. Hiyamizu, S. Shimomura, A. Wakejima, S. Kanedo, A. Adachi, Y.Okamoto, N. Sano, and K. Murase, J. Vac. Sci. Technol. B 12, 1043(1994).

13. K. Shinohara, S. Shimomura, and S. Hiyamizu, Jpn. J. Appl. Phys., Part 138, 5037 (1999).

14. K. F. Longenbach and W. I. Wang, Appl. Phys. Lett. 59, 2427 (1991).

15. W. I. Wang, E. E. Mendez, T. S. Kuan, and L. Esaki, Appl. Phys. Lett. 47, 826 (1985).

16. W. I. Wang, Surf. Sci. 174, 31 (1986).

Chapter 6

Midinfrared InGaAsSb quantum well lasers with digitally grown tensile-strained AlGaAsSb barriers

6.1 Introduction

InGaAsSb/AlGaAsSb quantum-well (QW) lasers have achieved good device performances and become the dominant choice in the 2–3 μm wavelength range.[1−5] Recently, we proposed and fabricated InGaAsSb/AlGaAsSb strain compensated multiple-quantum-well (SCMQW) structure by introducing more arsenic than that in conventional AlGaAsSb barrier latticed-matched to GaSb substrate.[6,7] Figure 6.1 shows the schematic band diagram of InGaAsSb/AlGaAsSb SCMQW laser structure. Due to its better hole confinement and more allowable compressive strain in the well,[6] the InGaAsSb laser diodes based on the SCMQW structure demonstrated improved performances such as higher differential quantum efficiency (DQE), higher characteristic temperature (T_0), and longer emission wavelength than those with conventional lattice-matched AlGaAsSb barriers.[6,7]

In this chapter, the optimization of molecular-beam epitaxy (MBE) growth for InGaAsSb SCMQW lasers was investigated to further improve the device performance and growth reliability. Specifically, short-period $(\mathrm{AlGaAsSb})_y$ / $(\mathrm{AlGaSb})_{1-y}$ digital barriers were employed during the MBE growth of the SCMQW active region. As a result, a low threshold current density of 163 A/cm^2 at room temperature was achieved for 1000-μm-long lasers emitting at 2.38 μm. An external DQE as high as 61% was obtained for the 880-μm-long lasers, the highest ever reported for any lasers in this wavelength range.

6.2 Experiments

All the samples were grown in a GEN-II solid-source MBE chamber equipped with As and Sb cracker sources. The growth structures were characterized by reflection high-energy electron diffraction (RHEED), high-resolution x-ray diffraction (HRXRD), and room-temperature photoluminescence (PL). HRXRD measurements were carried out with a Philips five-crystal x-ray diffractometer in the (400) crystal plane. Room-temperature PL measurements were performed using a 514.5 nm Ar+ laser, a Bomen DA8 Fourier transform infrared spectrometer, and a liquid-nitrogen-cooled InSb detector. Broad-area lasers based on InGaAsSb SCMQW were fabricated using AuZn and AuGe/Ni metallizations for the p- and n-type contacts. The laser performance were characterized by light-current (*L-I*) and wavelength measurements under various heat-sink temperatures.

6.3 Results and Discussions

6.3.1 Growth of InGaAsSb SCMQW

In InGaAsSb/AlGaAsSb SCMQW, the tensile-strained (TS) AlGaAsSb barriers have higher As composition than in traditional AlGaAsSb barriers lattice matched to GaSb substrate. However, the As composition (6%–10%) in the tensile-strained AlGaAsSb barriers is still lower than that (~15%) in the compressive-strained InGaAsSb wells, which generally requires different As beam fluxes for barrier and well layers. As a result, just as in the growth of InGaAsSb MQW structures with traditional lattice-matched AlGaAsSb barriers, the growth of InGaAsSb SCMQW with TS random alloy barriers requires pause at each barrier/well interface to adjust the As beam flux for different layers. However, in the digital-growth approach, the As shutter was not open all the time during the growth of the TS AlGaAsSb barrier.

Figure 6.2 shows the typical RHEED results for random-alloy and digital AlGaAsSb barriers. In contrast to the random-alloy approach, the adjustment of the average As composition in the TS AlGaAsSb was achieved by changing the duty cycle of the As shutter rather than by manually changing the As beam flux. Therefore, the As beam flux can be set at the point for the well growth and kept unchanged during the whole InGaAsSb/AlGaAsSb SCMQW growth. As a result, the growth interruption at the interfaces can be avoided completely. The reliability and reproducibility for the whole MBE growth procedure can be much improved, especially for MQW structures, by using the nonstop digital growth.

Optimizing the duty cycle of the As shutter in the AlGaAsSb growth is a key step for achieving high-quality InGaAsSb SCMQW. Figure 6.3 shows the XRD results of a set of four-period InGaAsSb(~20 nm)/AlGaAsSb(~10 nm) MQW samples with all the same growth

conditions except the As-shutter duty-cycle y in the digital $(Al_{0.25}Ga_{0.75}As_{0.145}Sb_{0.855})_y$ / $(Al_{0.25}Ga_{0.75}Sb)_{1-y}$ barriers. To imitate the growth interruption in the growth of the InGaAsSb MQW with quaternary AlGaAsSb random-alloy barriers, a 30 s pause was introduced at each barrier/well interface even though it could have been avoided completely.

When the As shutter was kept closed (i.e., y=0%) for the whole barrier growth time, the barrier became a compressive-strained ternary $Al_{0.25}Ga_{0.75}Sb$ random alloy and strain compensation did not exist in the MQW structures. No QW satellite peak was observed in the higher angle of the GaSb substrate peak, as shown in the top curve of Fig. 6.3.

With the increase of the As duty cycle from 0% to 100%, the principal QW satellite peaks began to appear on the right side of the GaSb (400) peak and gradually shifted toward higher angles, indicating that the average As composition increased as did the average tensile strain in the AlGaAsSb barriers. The full width at half maximum (FWHM) values of the highest principal QW peaks on the left side of the GaSb (400) peak, the average composition, and the average strain of the AlGaAsSb barriers were summarized in Table I. A very large value of 277 arc sec was measured for the MQW with compressive-strained $Al_{0.25}GaSb$ barriers due to the absence of strain compensation, which suggests strain relaxation in the MQW structure. The accompanied tensile strain caused by the incorporation of As in the barrier compensated the large compressive strain (1%–2%) in the well and prevented the strain relaxation of the whole MQW structure, as evidenced by the remarkable decrease of the FWHM values in the MQW with As duty cycles of 50% and 67%. However, the FWHM value increased significantly from 150 to 253 arc sec with the increase of y from 67% to 100%, indicating that the strain relaxation could

also occur in the thick tensile-strained AlGaAsSb barriers with large mismatch (e.g., -1.75% with the As shutter open all the time).

One issue with this series of InGaAsSb SCMQW samples shown in Fig. 6.3 was that the interface quality needed to be improved. According to the XRD theory on MQW structures with a period number of N, N−2 secondary QW peaks should be observable between the principal QW peaks if the QW interfaces were sharp and no strain relaxation happened in the MQW.[8] Our control experiment for the interface growth interruption proved that the poor interface quality was caused by the growth interruption at the QW interface.

Figure 6.4 shows the significant improvement of interface quality achieved by avoiding the growth interruptions. When all the growth interruptions at the QW interfaces were removed from the growth of four-period InGaAsSb SCMQW with 50% As duty cycle in the barriers, the secondary QW peaks appeared clearly (second curve) and the FWHM decreased from 185 arc sec (top curve) to 140 arc sec (second curve). Furthermore, high-quality InGaAsSb SCMQW with a period number as high as 8 was obtained by avoiding the growth stop. Clear secondary QW peaks symmetrically distributed between the principal ones were observed and the FWHM of 73 arc sec (third curve), which is very close to the ideal value of 72 arc sec (bottom curve), was obtained. In addition, the advantage of the nonstop growth was also confirmed by room-temperature PL. As shown in Fig. 6.5, the peak intensity increased by 50% and the FWHM decreased by 25% in the InGaAsSb SCMQW when the interface growth stop was removed.

6.3.2 InGaAsSb lasers with digital barriers

Based on the growth conditions developed for the previous high-quality InGaAsSb SCMQW with digital barriers, broad-area lasers, including InGaAsSb strain-compensated double quantum wells, were fabricated by using AuZn and AuGe/Ni metallizations for the p- and n-type contacts.[6,7] Laser bars with cavity length varying from 800 μm to 2 mm were cleaved and the facets were left uncoated. The laser performance was characterized under pulsed conditions (1 kHz repeating rate and 2 μs pulse width).

Figure 6.6 shows the *L-I* curve of the 1000 × 200 μm^2 laser bars and the lasing wavelength under room temperature at 28.5 °C. For these laser bars without lateral current confinement, a low pulsed threshold current density of 163 A/cm^2 with the lasing wavelength of 2.38 μm was obtained at room temperature. A slope efficiency of 150 mW/A for each uncoated facet was measured, which resulted in an external DQE of 58%. Figure 6.7 shows the high-temperature behaviors of the 880 × 250 μm^2 laser bars. As shown in Fig. 6.7(a), a record-high characteristic temperature (T_0) of 165 K was obtained up to temperatures as high as 80 °C while the T_0 value decreased significantly to 46 K with temperatures higher than 80 °C. The threshold current density for the lasers was still as low as 353 A/cm^2 at 80 °C.

The lasers can operate very well at temperatures higher than 100 °C and the maximum operating temperature was limited not by the measurement setup but rather by the lasing failure from the laser devices. At 20 °C, the lasers demonstrated a slope efficiency of 155 mW/A per facet, which corresponds to a record external DQE of 61%. The slope efficiency was reduced to 35 mW/A per facet at 100 °C, as shown in Fig. 6.7(b). However, the lasing performance was still very stable at 100 °C and the threshold current density was measured as low as 560 A/cm^2.

In addition, the emission wavelengths were compared between the SCMQW samples and the laser samples grown under the same QW growth conditions. A wavelength blueshift was always observed in the laser samples, possibly due to an annealing effect along with the 2.5 hour growth of the upper AlGaAsSb waveguide and cladding layers at 500 °C. The typical blueshift value shown in Fig.6.8 was measured as 38 meV, which could possibly be explained by the interdiffusion of the group-III atoms at the QW interfaces and the rearrangement of the group-V atoms inside the InGaAsSb wells.[9,10]

6.4 Summary and Conclusion

The growth interruption at the QW interfaces was shown to be responsible for the serious degradation of the interface quality during the InGaAsSb/AlGaAsSb MQW growth. $(AlGaSb)_x$ / $(AlGaAsSb)_y$ digital barriers were employed in InGaAsSb SCMQW to avoid the undesirable growth interruption, which in turn significantly improved the structural and optical properties as evidenced by XRD and PL measurements. Based on these high-quality SCMQW, a room-temperature threshold current density as low as 160 A/cm^2 was achieved for 1000-μm-long broad-area lasers emitting at 2.38 μm in pulsed mode. The 880-μm-long lasers could maintain high characteristic temperature of 165 K up to 80 °C and operate at a temperature higher than 100 °C. Compared to the SCMQW samples, a typical wavelength blueshift of 38 meV was observed in the laser samples most likely due to the annealing effect during the growth of the upper AlGaAsSb waveguide and cladding layers.

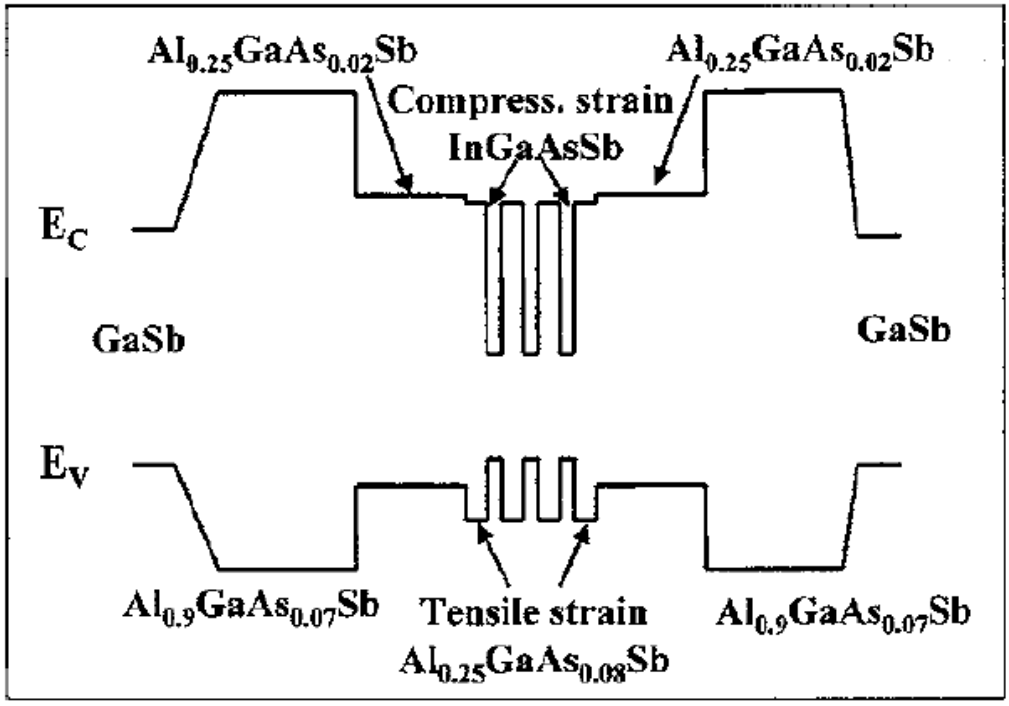

FIG.6.1 Schematic band diagram of InGaAsSb/AlGaAsSb SCMQW lasers.

Arsenic duty cycle (y) (%)	Ratio (AlGaSb:AlGaAsSb)	Average composition	Mismatch ($\Delta a/a_0$) (%)	FWHM (arc sec)
0	1:0	$Al_{0.25}GaSb$	0.32	277
50	1:1	$Al_{0.25}GaAs_{0.073}Sb$	−0.87	185
67	1:2	$Al_{0.25}GaAs_{0.097}Sb$	−1.06	150
100	0:1	$Al_{0.25}GaAs_{0.145}Sb$	−1.75	253

TABLE I. Summary of the AlGaAsSb digital barriers shown in Fig. 1.

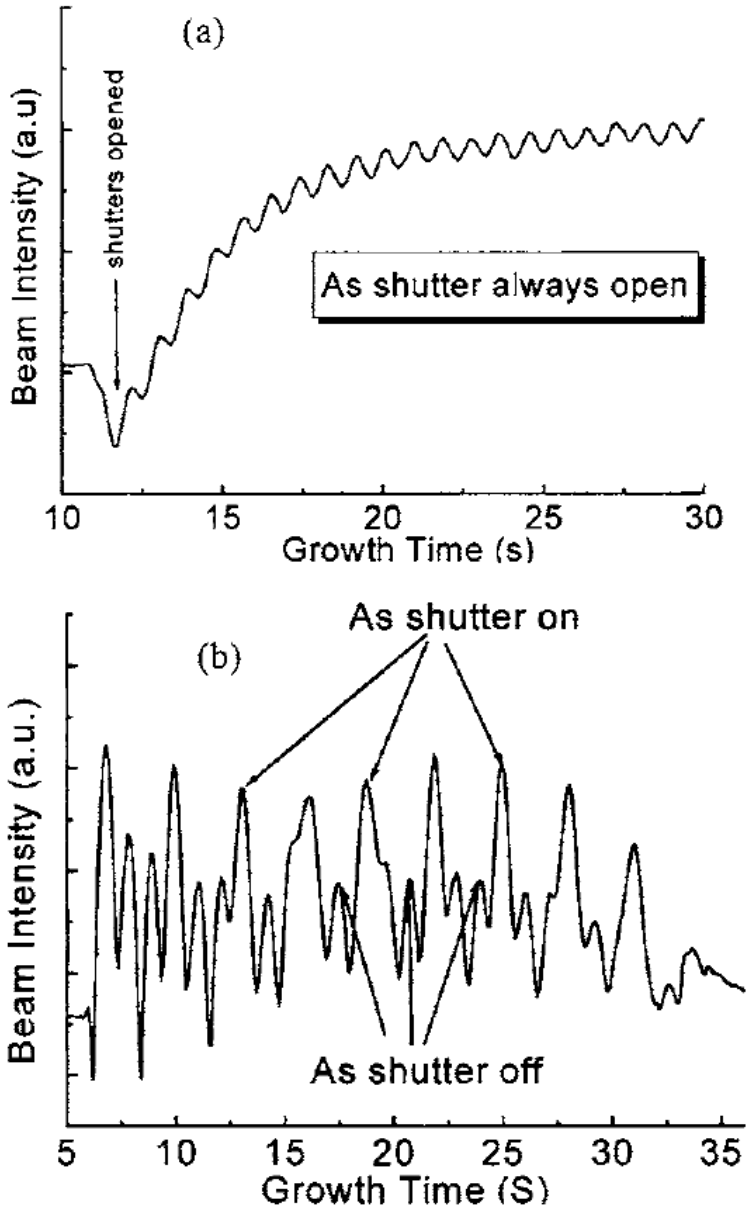

FIG.6. 2 Typical intensity oscillation of RHEED patterns during growth of (a) random-alloy and (b) digital-growth AlGaAsSb barriers.

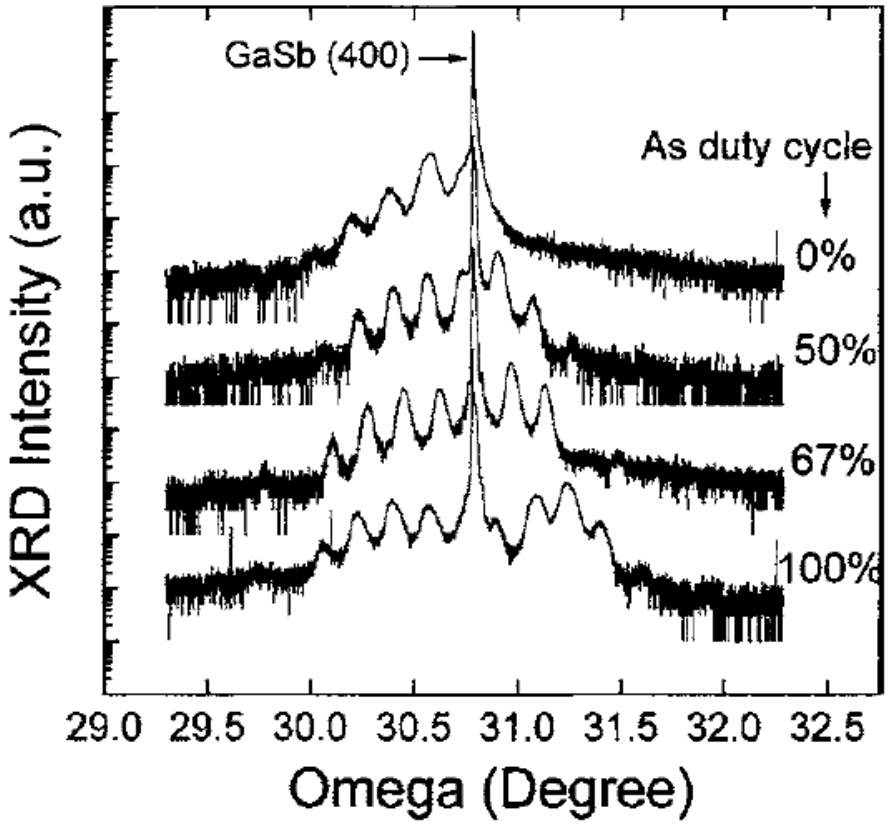

FIG. 6.3 XRD results of the InGaAsSb/AlGaAsSb MQW samples with $(Al_{0.25}GaAs_{0.145}Sb)_y$ / $(Al_{0.25}GaSb)_{1-y}$ digital barriers and 30 s growth interruption at each barrier/well interface. The XRD curves from top to bottom correspond to the As-shutter duty cycle y=0%, 50%, 67%, and 100%, respectively.

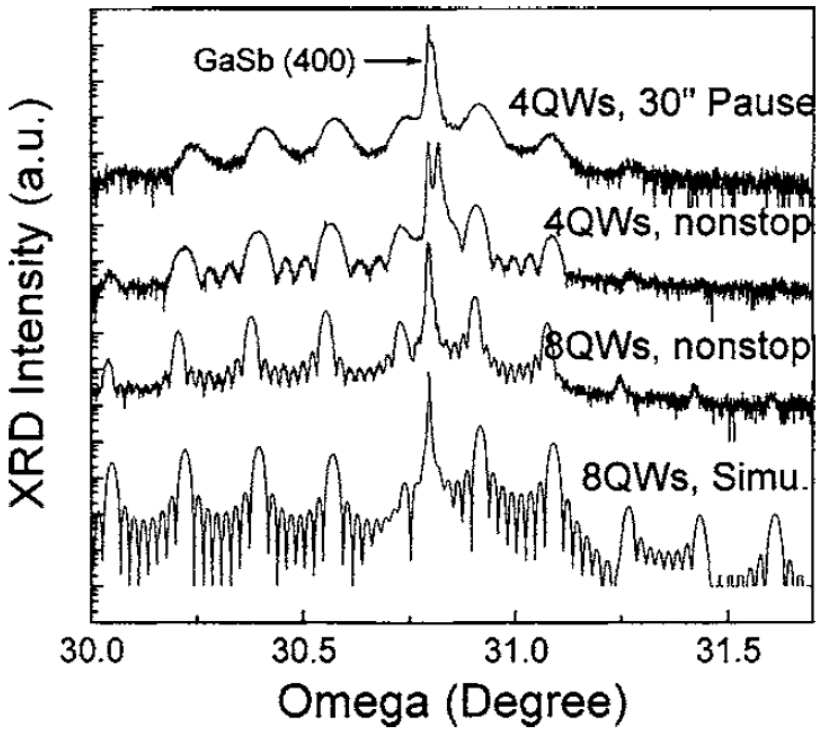

FIG. 6.4 XRD results of the InGaAsSb/AlGaAsSb SCMQW structures with four QW periods and 30 s interface pause (top curve), four QW periods and no interface pause (second curve), eight QW periods and no interface pause (third curve), and the simulation result of eight-period $In_{0.30}GaAs_{0.147}Sb$ (9.5 nm)/ $Al_{0.25}GaAs_{0.062}Sb$ (20 nm) SCMQW (bottom curve).

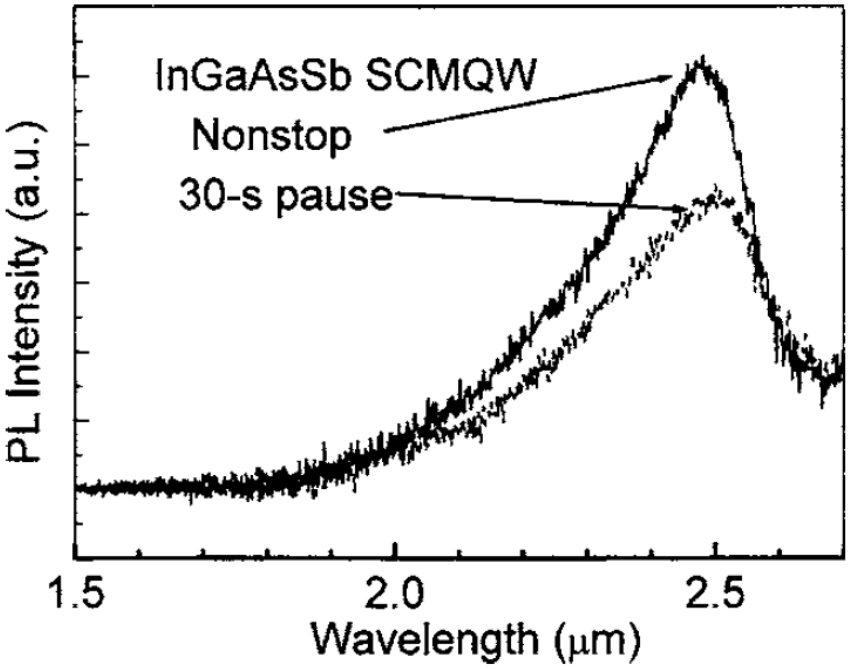

FIG. 6.5 Photoluminescence results of four-period InGaAsSb SCMQW with and without interface pause.

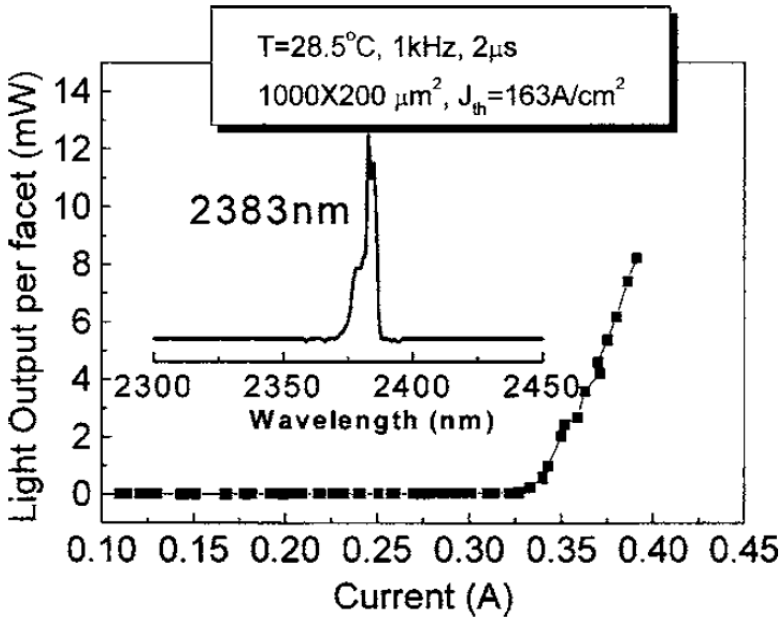

FIG. 6.6 Light-current curve and lasing wavelength of 1000 × 200 μm^2 double-quantum-well InGaAsSb/AlGaAsSb lasers under pulsed condition at 28.5 °C.

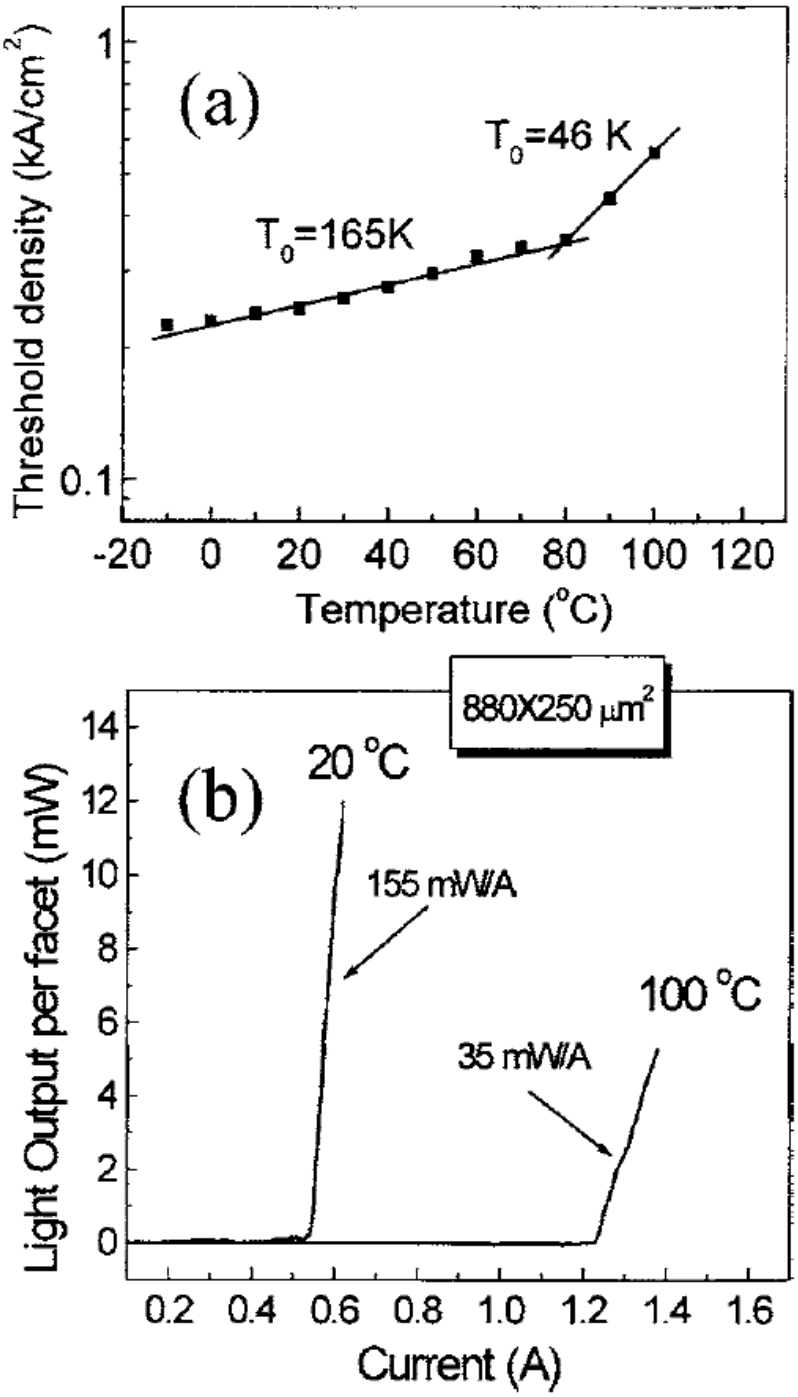

FIG. 6.7 Temperature dependence of (a) threshold current density and (b) the *L-I* curves under 20 and 100 °C for the 880 × 250 μm^2 InGaAsSb SCMQW lasers.

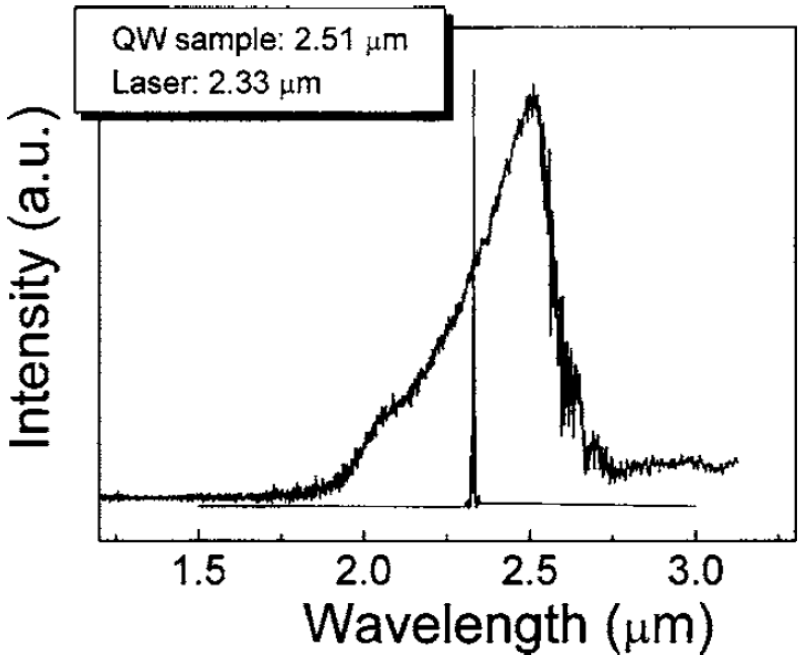

FIG. 6.8 Emission wavelengths of an InGaAsSb SCMQW-only sample and a laser sample under the same QW growth conditions. A blueshift of 38 meV was observed for the laser sample.

References

1. G. W. Turner, H. K. Choi, and M. J. Manfra, Appl. Phys. Lett. 72, 876 (1998).

2. J. G. Kim, L. Shterengas, R. U. Martinelli, G. L. Belenky, D. Z. Garbuzov, and W. K. Chan, Appl. Phys. Lett. 81, 3146 (2003).

3. D. Z. Garbuzov, R. U. Martinelli, H. Lee, F. K. York, R. J. Menna, J. C. Connolly, and S. Y. Narayan, Appl. Phys. Lett. 69, 2006 (1996).

4. H. Lee, P. K. York, R. J. Menna, R. U. Martinelli, D. Z. Garbuzov, S. Y. Narayan, and J. C. Connolly, Appl. Phys. Lett. 66, 1942 (1995).

5. M. Grau, C. Lin, and M. C. Amann, Electron. Lett. 38, 1678 (2002).

6. W. Li, J. B. Héroux, H. Shao, and W. I. Wang, Appl. Phys. Lett. 84, 2016 (2004).

7. W. Li, J. B. Héroux, H. Shao, and W. I. Wang, IEEE Photonics Technol Lett. 17, 531 (2005).

8. C. R. Wie, Mater. Sci. Eng., R. 13, 1 (1994).

9. C. S. Peng, J. Konttinen, H. F. Liu, and M. Pessa, IEE Proc.: Optoelectron. 151, 317 (2004).

10. 10K. Kim and A. Zunger, Phys. Rev. Lett. 86, 2609 (2001).

Chapter 7

Conclusion

This thesis demonstrated fabrication and characterization of infrared optoelectronic devices based on III-V compound semiconductors grown by Molecular Beam Epitaxy (MBE) utilizing various combinations of novel III-V materials, device structures and substrate orientations. The novel semiconductor lasers and photodetectors structures and materials investigated in this thesis cover the spectral range from 1.3μm to 12μm. This spectral region includes near-infrared (NIR), mid-infrared (MIR) and long wavelength infrared.

This thesis presented in two parts, the first part focused on two types of photodetectors; type-II InAs/GaSb superlattice IR detector (Chapter 2), and AlGaAsSb/InGaAsSb mid-infrared heterojunction p-i-n photodetector (Chapter 3). The second part of this thesis focused on the three types of quantum well (QW) lasers; phosphor-free1.3 μm InAlGaAs strain-compensated multiple-quantum-well (SCMQW) lasers on InP (100) (Chapter 4), InGaAsNSb/GaAs quantum wells (QWs) grown on GaAs (411)A substrates (Chapter 5), and mid-infrared InGaAsSb lasers with digitally grown tensile-strained AlGaAsSb barriers (Chapter 6).

We first introduced a historical prospective and motivation of research on optoelectronics devices based on III-V materials for infrared applications in Chapter 1. In Chapter 2, the type-II InAs/GaSb superlattice IR detectors with various spectral ranges were grown by MBE was discussed. Two superlattice structures with 15 monolayers (ML) of InAs/12ML GaSb and 17ML InAs/7ML GaSb are discussed. Based on X-ray diffraction (XRD) measurements both InAs/GaSb superlattices exhibit excellent material qualities with the full width at half maximum (FWHM) of the 0th-order peak about 20arcsec, which is among the narrowest ever reported. The 50% cutoff wavelengths at 80K of the two photodiodes with 15ML InAs/12ML GaSb and 17ML InAs/7ML GaSb superlattices are measured to be 10.2μm and 6.6μm, respectively.

In Chapter 3, the Mid-infrared heterojunction p-i-n photodetector, AlGaAsSb/InGaAsSb lattice-matched to GaSb grown by solid source molecular beam epitaxy was discussed. Using As and Sb valved crackers greatly facilitated the lattice-matching of the quaternary InGaAsSb absorbing layer to the GaSb substrates, as characterized by X-ray diffraction. The resulting device exhibited low dark current and a breakdown voltage of 32V at room temperature. A record Johnson-noise-limited detectivity of 9.0×10^{10} cm $Hz^{½}$ /W was achieved at 290K. The 50% cutoff wavelength of the device was 2.57 μm. Thus, our result has clearly demonstrated the potential of very high-performance lattice-matched InGaAsSb p–i–n photodetectors for mid-infrared wavelengths.

In Chapter 4, phosphor-free1.3μm InAlGaAs multiple-quantum-well (MQW) lasers was discussed, the substrate temperature has been found to be a critical growth parameter for lattice-matched InAl(Ga)As layers in the laser structures. Based on photoluminescence (PL) measurements, a large band gap reduction of 300 meV and a broadened PL peak were observed for the $In_{0.52}Al_{0.48}As$ layers with SL, as compared to those without SL. This results in a high laser performance. Threshold-current density as low as 690 A/cm² and T_0 as high as 80 K were achieved.

In Chapter 5, the interface and optical properties of InGaAsNSb/GaAs quantum wells on GaAs (411) substrates by molecular beam epitaxy was discussed. The InGaAsNSb/GaAs QWs on GaAs (411)A exhibited remarkably enhanced photoluminescence efficiency compared with the same structures on conventional GaAs (100) substrates.

Lastly, in chapter 6 the digital-growth approach for tensile-strained AlGaAsSb barriers was discussed. The digital-growth approach improved the reliability and controllability of MBE

growth for the MQW active region in the mid-infrared InGaAsSb quantum well lasers. The optical and structural qualities of InGaAsSb MQW were improved significantly, as compared to those with random-alloy barriers due to the removal of growth interruption at the barrier/well interfaces in digital growth